A Study of Some Contemporary Issues in Electron Devices:
Electrical contact, heating, and amplifier stability

by

Foivos Antoulinakis

A dissertation submitted in partial fulfillment
of the requirements for the degree of
Doctor of Philosophy
(Nuclear Engineering and Radiological Sciences)
in the University of Michigan
2020

Doctoral Committee
  Professor Yue Ying Lau, Chair
  Professor Mark Kushner
  Professor Ryan McBride
  Professor Alec Thomas

Foivos Antoulinakis
foivos@umich.edu
ORCID iD: 0000-0003-2864-5305

Acknowledgements

First and foremost I would like to thank Professor Y. Y. Lau for a multitude of things he has done that were imperative to this work. He believed in me enough to admit me as his student and never stopped believing in me, which required immense patience at times. He has taught me countless things and guided me in the right direction to solve diverse problems in many situations. He has also provided many stimulating problems to ensure I would never lose interest in this field. I also like to thank Professors Ryan McBride, Mark Kushner, and Alec Thomas, for serving on my thesis committee. I would like to thank Professor Peng Zhang of Michigan State University. Not only did he pave the road to developing a theory on AC contact resistance, he also was the one who mentored me in my first year as a graduate student which set me up for success. Furthermore, I thank Professor Ryan McBride for taking me on as a graduate student instructor on his first time teaching the Plasma Generation and Diagnostics Laboratory, which taught me a great deal not only about plasma physics but also the difficulties of the experimental process. I would also like to thank my fellow graduate student Paul Campbell for enlisting my help building B-dots which taught me the intricacies of making magnetic field measuring devices by hand.

I would also like to thank all of the Professors in the Nuclear Engineering and Radiological Sciences Department who taught me a great deal in class. I would specifically thank my graduate coordinator Garnette Roberts who has been an immense help by patiently informing me of the many procedures I needed to complete throughout my PhD that I would have overlooked otherwise.

Lastly I would like to thank all friends and family that indirectly supported me in this work. Without their love and support it would have been impossible to muster the willpower to complete this work. I believe it is necessary for a person to be able to momentarily forget about their everyday work in order to be better at it, especially when a fresh perspective can sometimes be all one needs to solve a difficult problem.

Table of Contents

List of Figures

List of Appendices

Abstract

This thesis presents a theoretical study of three fundamental topics of contemporary interest to electron devices: electrical contact resistance under AC condition, a nonlinear, steady state theory of thermal and electrical conduction on a one-dimensional conductor, and the absolute instability in a traveling wave tube.

Poor electrical contact is known to be a major cause of failures in all electrical/electronic systems, ranging from small scale consumer electronic devices to large scale military and aerospace systems. The quality of contact is often measured by the contact resistance, which has been treated mostly under steady state (DC) condition. This thesis considers the vastly more complex problem of AC contact resistance. By analyzing an AC current flowing through two Cartesian current channels, with different dimensions and different electrical resistivity, in contact with each other at an interface, the AC contact resistance as a function of frequency is calculated. Scaling laws are obtained and interpreted in terms of the degree of current crowding exhibited at the junction as a result of resistive skin effects in the respective current channels. Our AC results always reduce to the corresponding DC results under the low frequency limit where the resistive skin depths are much larger than the channel sizes. In some geometry and at some frequency, the AC contact resistance may become negative, meaning that the total AC resistance in the two current channels is less than the AC bulk resistances from the individual channels. The contact resistance on a slightly uneven joint is also evaluated as unique scalings of contact resistance was found with frequency. The mathematically divergent field at the sharp corner at the joint is given some attention, under AC condition.

The second problem concerns the degree of ohmic heating in a current-carrying conductor. We present a nonlinear, steady state, theory of thermal and electrical conduction on a 1-dimensional conductor using several models to specify the temperature dependence in the thermal and electrical conductivities. The temperature distribution is presented for each model, together with the parameter space for the existence of the steady state solutions. Nonexistence of a steady state solution may suggest the possibility of thermal runaway. The temperature distribution calculated according to the theory has been favorably compared with experiments on a field emitter made of a carbon nanotube fiber.

The last problem concerns the stability of a traveling wave tube (TWT) which is a central component in virtually all communications satellites. High mission demands require high power, at which stable operation of TWT may become an issue. This thesis examines an absolute instability in a TWT that could occur at the upper and lower edges of the amplification band. We use the Briggs-Bers criterion to confirm the previous findings on the existence of absolute instability at the upper band edge when the electron beam current that powers the TWT is sufficiently high. We correct the erroneous previous conclusion on the non-existence of absolute instability at the lower band edge. The temporal-spatial evolution of the Green's function was calculated. It corrob-

orated the above-mentioned results, and it shows, for the first time, transient exponential growth as a fractional power of time initially, followed by simple exponential growth in time or decay in time, depending on whether the current threshold for absolute instability is exceeded.

Chapter 1. Introduction

This thesis is a theoretical study of three problems which originated from the author's study of high power microwave sources. High power microwaves have many applications in radar, communication, national defense and homeland security, industrial processes, and accelerator developments [1, 2]. The first problem studied in this thesis concerns the electrical contact resistance, under AC condition, between two current-carrying channels. The second problem concerns the temperature distribution in a current-carrying conductor whose electrical resistivity and thermal conductivity may depend on the temperature. The third problem concerns the stability of a traveling wave amplifier near the edges of its amplification band. The background of each of these three problems is described in each subsection below. The outline of this thesis is given towards the end of this Chapter.

1.1   Background on AC Contact Resistance

Contact problems account for 40 percent of all electrical/electronic failures, ranging from small scale consumer electronic devices to large scale military and aerospace systems [3–5]. In pulsed power systems and high power microwave sources, poor electrical contact prevents efficient power coupling to the load [6], produces unwanted plasma [7], and even damages the electrodes. On the largest scales, faulty electrical contact has caused failure of the Large Hadron Collider, and similarly threatens the International Thermonuclear Experimental Reactor [8]. On the smallest scales, electrical contact and local heating are very important issues in microelectronics [9, 10], integrated circuits [10], thin film devices [11], carbon nanotube [12, 13] and carbon nanofiber based cathodes [14, 15] and interconnects [10, 16–19], field emitters [20, 21], thin film-to-bulk contacts [22–27], semiconductor nanolasers [28, 29], and ultrafast and nanoscale diodes [30–33].

The quality of a contact is often measured by the contact resistance [3, 4]. Despite its importance, contact resistance, and the enhanced ohmic heating that results, have been treated mostly under steady state (DC) condition [3, 4, 34–40]. The evaluation of contact resistance in the AC case is significantly more complex than the DC case. New features, such as resistive skin effect, inductive, and capacitive effects, as well as radiation losses, are totally absent in a DC theory. For the AC case, the simple "a-spot" geometry has received some attention [35, 36, 41–43]. (The a-spot geometry refers to two current channels, made of the same materials, joined with each other only through a circular hole of radius a [3, 4]). A statistical theory for a collection of asperities at the interface of two conductors under AC condition was given by Tang et al. [44], who ignored the all-important skin effects, and the effects of dissimilar materials.

This thesis studies the contact resistance between two channels through which an AC current passes. The current channels may assume different dimensions and different electrical properties. We discovered several unusual proper-

ties of the AC contact resistance [45]. We present novel scaling laws at various frequencies.

1.2 Background on Effects of Temperature Dependence of Electrical and Thermal Conductivities on the Joule Heating of a Conductor

Crowding of the current flow at the junctions of electrical contact contributes contact resistance, whose presence leads to enhanced local heating [3, 4]. Such enhanced local heating is detrimental to the performance and to the integrity of devices. The local rise in temperature may lead to a local change in the electrical and thermal conductivity, which in turn leads to a re-distribution of the current flow pattern at the contact, and therefore to a change in the contact resistance. This feedback may result in an "electrothermal instability" [46–49] and in the worst case, to a thermal runaway - local heating may reduce the electrical conductivity which contributes to further heating and eventual device failure. The inclusion of the temperature dependence in the evaluation of contact resistance is a very complicated problem, and to the author's knowledge, was never attempted. To isolate the physics in the current distribution and the resulting change in the temperature profile due to the temperature dependence in the electrical conductivity (σ) and in the thermal conductivity (κ), we study the reduced problem of a 1-dimensional conductor, under the steady state assumption [50]. This work was published and was later used (by others) to interpret the recent experiments on field emitters that were performed at the Air Force Research Laboratory [51]. This problem of enhanced Joule heating at junctions is of broad interest, as given in the following survey.

Recent advancements in nanotechnology, the miniaturization of electronic devices, and the increase in density of circuit integration, make Joule heating increasingly important to device performance and lifetime. The growing packing density and power consumption of very large scale integration (VLSI) circuits in particular have made thermal effects one of the most important concerns of VLSI designers [52]. In micro-electro-mechanical (MEM) switches, the durability of the devices is largely limited by Joule heating at the contacting asperities [26, 35]. Coupled thermal-electrical effects play important roles in current emission performance as well as the stability of carbon nanofiber based field emitters [12, 14, 15, 53]. There has also been interest in understanding and controlling the local temperature increases within electrically driven nanoscale wires and metallic interconnects [54]. Thermal stability is one of the key challenges in nanoscale devices made of novel materials, such as graphene [55–57] and organic materials [58, 59]. In electrically pumped nanolasers for chip-scale optical communications, thermal management is of crucial importance to realize room temperature operation [28, 60].

The coupled thermal-electrical conduction problem is also important in many other areas such as wire-array Z-pinches [6], power transmission lines [61], high power microwave devices [62, 63], and electrical contacts [4, 40, 43, 64, 65].

In a Z-pinch, in particular, coupled thermal-electrical conduction is responsible for an electrothermal instability which was extensively studied in recent years [46–49].

Available 3D finite element simulation codes may be used to compute the effects of coupled electrical and thermal conduction with great accuracy. However, the parametric dependencies of the solution are difficult to determine from such purely numerical calculations. Here, by using a very simple 1D model, we aim to provide a better understanding of the underlying physics and the influences of multiple parameters on key properties of the solution, including the domains for the existence of solutions, and the maximum temperature and its location in the 1D conductor when a steady state solution exists. Our 1D result was successfully used to interpret the temperature distributions in carbon nanotube fibers experiments [51].

1.3 Background on Absolute Instability in a Travelling Wave Tube

Traveling wave tubes (TWTs) are widely used in satellite communication and in radar (Fig. 1.1) [1, 2, 66–68]. To amplify a signal of frequency, ω, which may range from GHz to THz for TWT, the kinetic energy of an electron beam is converted to the signal's electromagnetic wave energy through a collective interaction. If this interaction is too strong, the amplifier becomes unstable and breaks into oscillation, defeating the TWT function. Stability of TWT is thus a major concern [67–73], and this thesis studies one aspect of this problem, known as the absolute instability [74, 75]. To understand the nature of TWT stability, consider an electron beam propagating in the z-direction with velocity v. For this beam to convert its kinetic energy to the signal so that the signal is amplified, it must be made to interact strongly with the signal's electromagnetic wave, represented in the form, $e^{i\omega t - ikz}$. This signal also propagates in the z-direction with wavenumber k, $k = k(\omega)$, which is a function of the signal frequency. Strong interaction between the beam with the electromagnetic wave can occur only when the wave's phase velocity, ω/k, is roughly equal to v (Fig. 1.1 [66–68, 76, 77]. The relation, $\omega/k = v$, is thus known as the beam mode in plasma physics, and it is represented by a straight line in the ω-k plane (Fig. 1.2). Since the speed of light in vacuum is c, which always exceeds v, for the phase speed along the z-direction to be equal to v ($< c$), the electromagnetic circuit on which the signal propagates needs to have a so-called slow-wave structure (SWS), properly designed so that the z-component of its phase velocity (ω/k) is less than c [66–68]. Commonly used SWS for TWT include a metallic wire wound into to a helix (Fig. 1.1) [66–68, 78, 79], coupled-cavity [66, 68], a rectangular waveguide bent into a serpentine shape in the direction of propagation [80], and more recently, metamaterials are also considered as a candidate of SWS for TWT [81]. Note that all of the above SWS are periodic in z. Their dispersion diagram, known as the circuit mode in the ω vs k plot, is a periodic function of k with period $2\pi/L$, where L is the periodicity in the SWS (Fig. 1.2) [66, 68]. Strong interaction occurs when the phase velocity of

the circuit mode coincides with the beam velocity, such as the point Q in Fig. 1.2 [66, 68, 70, 76].
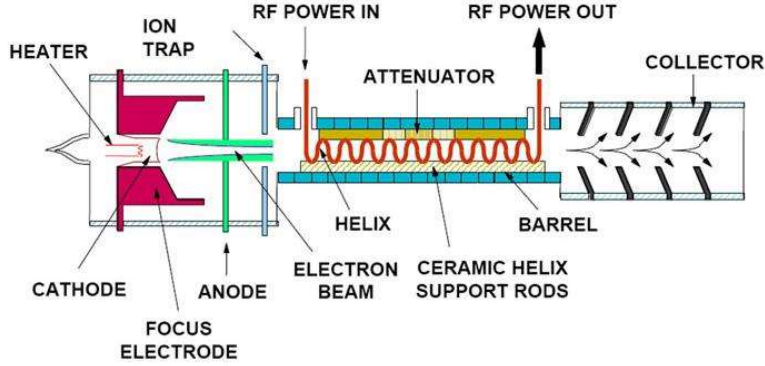
Figure 1.1: A schematic of a taped helix TWT. An electron beam is generated and accelerated within the ion trap and a microwave signal is input at "RF power in". This signal is forced to travel along the helix which matches its axial velocity to the velocity of the electron beam. The electron beam is modulated and transfers some of its kinetic energy to the microwave signal, amplifying it. The microwaves are then extracted, and some of the remaining electron beam energy is recovered in the collector. From [82]

Only signal frequencies within certain bands can propagate on a SWS, and these are called the pass bands [66, 68]. One such pass band is shown in Fig. 1.2, where frequencies between ω_L and ω_U can propagate. These two frequencies are respectively designated as the lower and upper band edges, within which a signal could be amplified. Note that at these band edges, the group velocity of the circuit wave equal to zero, making the circuit difficult to match at ω_L and ω_U. Thus, oscillations at either band edges are distinct possibilities and, indeed, band edge oscillations are a major threat to the operation of TWT [69–71, 73, 83–85].

It is a common experience that an amplifier becomes unstable if its gain is too high. This is also true for a TWT. Qualitatively, the gain at frequency ω is measured by $k_i(\omega)$, where k_i is the imaginary part of the wavenumber $k(\omega)$, which is to be solved from the TWT dispersion relation, written generally in the form [66–68, 76, 77]

$$D(\omega, k) = 0 \tag{1.1}$$

The amplitude of the signal of frequency ω then achieves amplification equal to $\exp(k_i z)$ after propagating a distance z along the TWT, *provided the amplifier is stable*. If the TWT is unstable, the unstable solution with temporal growth rate ω_i would be excited, and this temporally growing solution would overwhelm the sinusoidal steady state solution $\exp(i\omega t - ik(\omega)z)$ that is associated with the input signal of frequency ω.

4
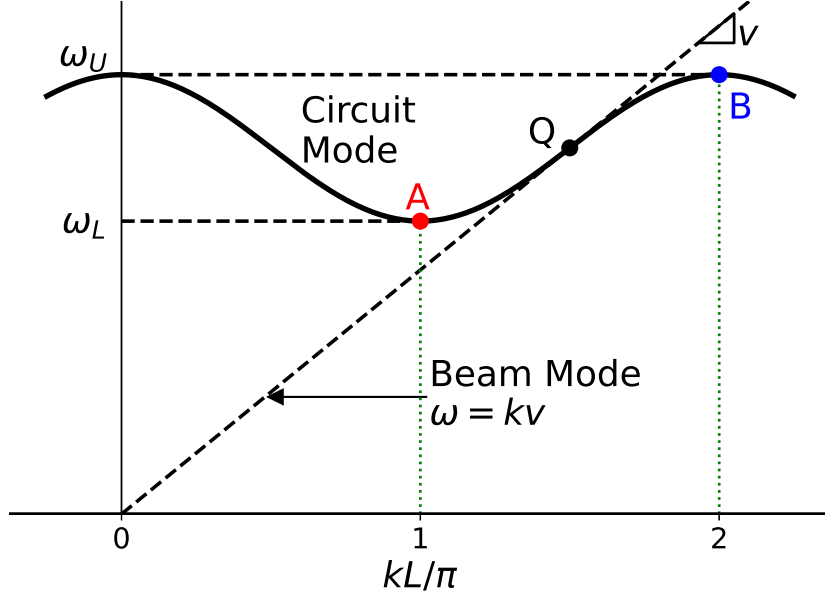
Figure 1.2: Lower band edge (A), the upper band edge (B), and the operating point (Q) at which the beam mode intersects with the circuit mode in a coupled cavity TWT at $(\omega, k) = (\omega_0, k_0)$. kL is the phase shift per period of the slow wave structure.

The dispersion relation (1.1) is obtained from consideration of the collective interaction between the beam mode and the circuit mode [66–68, 76]. To determine if the system described by the 1-dimensional dispersion relation (1.1) exhibits a natural solution that is exponentially growing or decaying in time, one needs to consider an initial value problem (like the study of Landau damping in plasma physics [77]). Specifically, we examine the Green's function, which may be written in the form [74, 75, 77],

$$G(z,t) = \int d\omega \int dk \frac{e^{i(\omega t - kz)}}{D(\omega, k)} \tag{1.2}$$

Eq. (1.2) represents the natural response due to an impulse excitation in time and in space. The k-integration is along the real k axis, and the ω-integration is carried along the Bromwich contour in the theory of Laplace transform [74, 75, 77]. Briggs and Bers [74, 75] established a mathematical procedure, known as the Briggs-Bers criterion, that determines the condition under which Eq. (1.2) exhibits unstable solution that grows exponentially with time. [The Briggs-Bers criterion will be summarized in Section 4.2 below.] If it does, then an absolute instability exists. This instability is termed "absolute" because at every point, z, the Green's function asymptotically grows exponentially with time, at a constant growth rate. If the system is not absolutely unstable, it may still

be convectively unstable, meaning that the Green's function, at a fixed position z, grows transiently in time before it decays asymptotically. The convectively unstable system has some gain mechanism (for presence of transient growth of disturbances), but the transient solution eventually decays in time. Hence it makes sense to talk about the sinusoidal steady response due to an input signal of frequency ω, and to evaluate the spatial amplification rate of the signal amplitude, $k_i(\omega)$, for real omega from Eq. (1.1) for the wave solution of the form $\exp(i\omega t - ik(\omega)z)$. In fact, TWT operates properly only in the convectively unstable regime, so that the amplifier will have gain, yet operating stably. The system is stable, i.e., it has neither absolute nor convective instability, if for all real values of k, the solutions of ω that solve the dispersion relation Eq. 1.1 do not have a negative imaginary part [74, 75, 77].

The Briggs-Bers criterion [74, 75] has been applied to TWT models to examine both the absolute instability both at the upper band edge (B) and at the lower band edge (A), shown in Fig. 1.2, when the operating point (Q) is away from both band edges. Previous investigations [69, 70, 73, 83] conclude that the upper band edge (A) may be subjected to an absolute instability when the electron beam current is sufficiently high. They also conclude that the lower band edge is not subjected to an absolute instability, regardless of the beam current [69, 70, 83]. In this thesis, we point out that the last conclusion on the lower band edge is incorrect. When we tried to assess the transient growth at the lower band edge, we discovered that the lower band edge may be subjected to an absolute instability if the beam current is sufficiently high. This conclusion was also corroborated by our careful analysis of the Briggs-Bers criterion for the lower band edge. In addition, our Green's function solution shows, for the first time, the transition from transient exponentiation at fractional power of time to simple exponential growth (to decay) when the band edge is (is not) subject to an absolute instability. Finally, we remark that absolute instability in a TWT is very difficult to detect experimentally, as addressed toward the end of Chapter 4.

1.4   Organization of Thesis

The three topics, AC contact resistance, temperature distribution in a 1-D conductor on which the thermal and electrical conductivity depend on temperature, and absolute instability in TWT, will be given in Chapters 2, 3, and 4 respectively. In Chapter 2, we describe in Section 2.1 the model under consideration for the AC contact resistance. The proper definition of AC contact resistance is defined in Section 2.2, so that the low frequency limit is consistent with the established DC theory. Section 2.3 gives numerical examples for various geometries, including the discovery of "negative contact resistance", and the scaling laws as the frequency increases. In virtually all cases under study, we give a physical interpretation of the scaling in the contact resistance in terms of current spreading (or current constriction) in the vicinity of the contacting regions. Section 2.4 presents our preliminary examination of the "triple point" under AC condition. Here, the triple point is the location where two current channels

and the surrounding vacuum meet, and where the mathematical solutions for the electric field diverge. Section 2.5 gives an assessment of capacitive effects. Section 2.6 summarizes the results of AC contact resistance.

Chapter 3 solves the steady state temperature distribution on a 1-dimensional conductor whose electrical conductivity (σ) and thermal conductivity (κ) may be functions of temperature (T). Section 3.1 presents the governing equations and their scaling to reduce the parameter space. Section 3.2 presents the exact and numerical solutions for various models of $\kappa(T)$ and $\sigma(T)$, including linear dependence, and those obtained empirically from experiments. Boundaries on the existence of the solutions are given, together with comparison of the theory with experiments. Section 3.4 presents a summary of the results.

Chapter 4 considers the absolute instability and the transient growth near the upper and lower band edge of a TWT. Following the introduction in Section 4.1, Section 4.2 presents our analysis of the Briggs-Bers criterion on both the upper and lower band edges, where the previous erroneous conclusion regarding the lower band edge is pointed out. Section 4.3 presents the transient growth of the Green's function, which we discover to be in the unusual form of growth at fractional power of time, $\exp(A\omega t^{1/3})$, at early times. At later times this Green's function grows into the simple exponential form $\exp(\omega_i t)$ when an absolute instability exists, or decays to zero when the TWT is convectively unstable. Here, A is a constant (in time) but it depends on z. Section 4.4 summarizes the result. Chapter 5 concludes the thesis and suggests future works.

Some of the detailed derivations in Chapters 2, 3, and 4 are given in the Appendices.

Chapter 2. A Theory of Contact Resistance Under AC Conditions

Section 2.1 gives the introduction. In Section 2.2, we shall first outline the model for the DC contact resistance, concentrating on its salient properties that will be useful in the extension to the AC case, which is described next. In Section 2.3, we shall present a few examples of the AC contact resistance, where the novel scalings are presented. Section 2.4 considers the mathematical treatment of the divergent solutions at a triple point. Section 2.5 gives a rudimentary evaluation of the low frequency capacitive effects via an example. Concluding remarks are given in Section 2.6. The details of the derivation of the novel scalings will be given in the Appendices.

2.1 Introduction

For this thesis, a theoretical study of AC electrical contact was initiated using the simple Cartesian geometry shown in Fig. 2.1, allowing for contacts between dissimilar materials. This seemingly simple geometry of two conducting channels turns out to be extremely difficult to analyze for the AC case. We adopted it because simple models more readily yield physical insights. In addition, in the DC limit, its field solutions and the contact resistance have been completely characterized by Zhang and Lau [64], and this reveals new features associated with the AC case. An AC current of frequency ω is launched from the left channel at large negative value of z, and it exits at the right channel at large positive value of z. The dimensions and the electrical properties (permittivity ε, conductivity σ, and permeability μ, all assumed real) are specified in Fig. 2.1. The two conducting channels, with an interface at $z = 0$, are surrounded by vacuum. We have formulated the boundary value problem for Fig. 2.1 which satisfies the Maxwell equations in the various regions, interior and exterior to the current channel. In this chapter, we shall restrict to the study of resistive loss at the contact in the regime $\sigma \gg \varepsilon\omega$ for both conducting channels. Under this assumption, we found that the current flow pattern within the current channel is essentially unaffected by the solution in the vacuum region, just like the DC case. We should stress that our solutions using this simplifying assumption has been spot-checked against the complete electromagnetic field solutions that we have constructed for all regions, both exterior and interior to the channel. We shall further comment on the general case towards the end of this section.
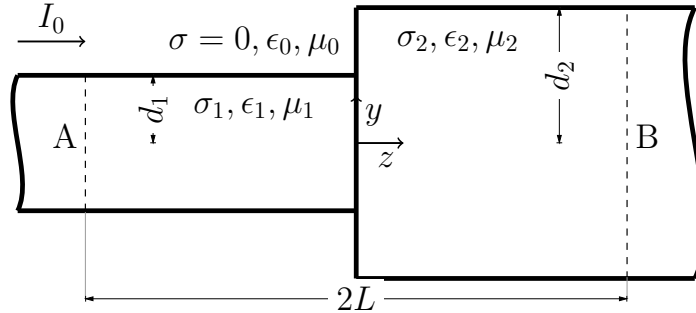
Figure 2.1: Two Cartesian current channels, each with length L and joined at $z = 0$, are surrounded by vacuum. An AC current of the form $I_0 e^{-i\omega t}$ enters the left surface A and exits the right surface B.

The two-dimensional, planar, model (Fig. 2.1) gives considerable physical insight into the nature of current crowding from DC to high frequency conditions. Similar to the DC case [64], we expect the qualitative features to hold for the cylindrical geometry. This study also reveals the deleterious effects of conductor misalignment on the contact resistance, especially at high frequencies. Modulation at 10 GHz and beyond is being pursued for nano light emitting diodes for on-chip optical communications [60], making high frequency AC contact resistance in that frequency range relevant.

The resistive skin depth $\delta = (2/\mu\omega\sigma)^{1/2}$ in each conducting region is an important length scale. It is frequency dependent. The relative magnitude of δ in the two different regions of the channel, and the transverse dimensions of the channels then strongly affect the current flow pattern. Therefore, different scalings for the AC contact resistance are expected for different frequency ranges. This chapter reports some such novel scalings. We interpret them by identifying the skin depth as the effective channel widths and then use the corresponding DC scalings.

2.2 Definition of Contact Resistance

For the Cartesian geometry shown in Fig. 2.1, we shall define the contact resistance, first for the DC case and then for the AC case. We assume that, in both cases, there is no variation in the x-direction, and the channel width in the x-direction is W, and that the channel axial length, L, is sufficiently large that the field solutions no longer have any z-variation at $z = \pm L$ for the bulk solution.

2.2.1 DC contact resistance

For the DC case, current I_0 with a constant, uniform current density, $I_0/(2Wd_1)$, enters from the left channel at plane A ($z = -L$). This current exits the right

9

channel at plane B ($z = L$) also with a constant, uniform current density, $I_0/(2Wd_2)$. A DC voltage V is needed to drive this current between planes A and B. The total resistance, R, between A and B is then,

$$R \equiv \frac{V}{I_0} = \underbrace{\frac{L}{2d_1 W \sigma_1}}_{\text{Bulk}} + \underbrace{\frac{\overline{R_c}}{4\pi W \sigma_2}}_{\text{Interface}} + \underbrace{\frac{L}{2d_2 W \sigma_2}}_{\text{Bulk}} \tag{2.1}$$

where the first (last) term on the RHS represents the bulk resistance of the left (right) channel. The middle term of Eq. (2.1) is defined as the contact resistance, or the interface resistance, which is simply the difference between the total resistance (R) and the bulk resistance of the two current channels. Note that this contact or interface resistance vanishes if $d_1 = d_2$, in which case the DC current flow (and the DC electric field, which is solely in the z-direction) is uniform in both channels, and the channels' bulk resistance, in series, constitutes the total resistance. Thus the contact or interface resistance in Eq. (2.1) is also called the spreading resistance (or constriction resistance), as it is a measure of how the current spreads (or constricts) as it approaches and leaves the junction [3, 4, 35, 36].

The contact resistance in Eq. (2.1) is represented by the normalized contact resistance $\overline{R_c}$. Zhang and Lau [64] found that $\overline{R_c}$ depends only on the ratios d_1/d_2, and σ_1/σ_2 (Fig. 2.1). They computed $\overline{R_c}$ from their exact electrostatic field solution that satisfy the following boundary conditions: (Fig. 2.1)

$$\sigma_1 E_{z,1} = \sigma_2 E_{z,2}, \qquad\qquad |y| < d_1, z = 0 \tag{2.2a}$$
$$E_{y,1} = E_{y,2}, \qquad\qquad |y| < d_1, z = 0 \tag{2.2b}$$
$$E_{z,1} = 0, \qquad\qquad d_1 < |y| < d_2, z = 0 \tag{2.2c}$$
$$E_{y,1} = 0, \qquad\qquad |y| = d_1, z < 0 \tag{2.2d}$$
$$E_{y,2} = 0, \qquad\qquad |y| = d_2, z > 0 \tag{2.2e}$$

Equations (2.2a) and (2.2b) show, respectively, continuity in the current flow and in the tangential electric field at the channel interface. Equations (2.2c) - (2.2e) state that there is no normal electric field at all channel-vacuum interfaces. That is, the conduction current always flows tangentially at the channel-vacuum boundary. Accurate scaling laws for $\overline{R_c}$ have been constructed from the numerical solutions of the electrostatic potential for Fig. 2.1, solved exactly using the boundary conditions (2.2a)-(2.2e). [64]

An alternative definition of the contact resistance uses the ohmic power dissipated within the current channel, which can be obtained from the calculated (AC and DC) field solution for Fig. 2.1. This approach is more suitable for the AC case, in which the "potential" on the surfaces A and B are no longer uniform or constant. For the AC case, the total resistance, R, in the channel may be expressed in terms of the average ohmic power dissipated within the channel,

$$P \equiv \frac{RI_0^2}{2} = \frac{1}{2} \int_{\text{volume}} \sigma |\boldsymbol{E}^2| dV \tag{2.3}$$

10

where $\boldsymbol{E}$ is the AC electric field over the channel volume, $-L < z < L$. The total resistance R obtained from Eq. (2.3) is then decomposed into the bulk resistance, R_{b1} and R_b2, associated with the channel, and the remainder is then defined as the contact resistance, R_c,

$$R = R_{b1} + R_c + R_{b2} \qquad (2.4)$$

For the DC case, R_{b1} and R_{b2} are given respectively by the first and third term in the RHS of Eq. (2.1). Comparing R_c, obtained from energy consideration (Eqs. (2.3) and (2.4)), and from the published results by Zhang and Lau [64] who used the exact electrostatic field solution without reference to ohmic loss, we obtain an excellent agreement between the two in several test cases.

2.2.2 AC contact resistance

For the AC case, the "potential" on the surfaces A and B in Fig. 2.1 is not defined, and we need to use the power dissipation formulation, Eqs. (2.3) and (2.4), for an unambiguous identification of the contact resistance. The conventional definition of potential difference as $\Delta\phi = \int \boldsymbol{E} \cdot d\boldsymbol{l}$ does not work when there are skin effects, since the electric field at $y = 0$ is different than the electric field at $y = d_1$, and therefore we would obtain different values for $\Delta\phi$ depending on the path we chose. It is possible to choose any gauge and solve for the potentials in this way, but there are no real benefits in doing so as the resistance will not easily arise from such potentials.

Like the DC case, the power P in Eq. (2.3) requires the field solution $\boldsymbol{E}$ everywhere within the channel (Fig. 2.1). However, for the AC case, the boundary conditions to be satisfied need to be modified from Eqs. (2.2a)-(2.2e). In general, $E_\parallel$ and $(\sigma - i\omega\varepsilon)E_\perp$ need to both be continuous across any boundary. This means that there can now be currents that flow into the conductor from the conductor-vacuum interfaces. This complicates the problem by a significant degree as fields outside the conductors now affect fields inside, and therefore need to be calculated. However, in this chapter we will focus on good conductors ($\sigma > 10^4$ S $\cdot$ m, $\varepsilon/\varepsilon_0$ of order unity) and frequencies of up to 1 THz. For these values we get $\omega\varepsilon \ll \sigma$ which allows us to ignore the fields in the vacuum once more, like the DC case, and use the same method of series expansion as in Zhang and Lau [64] to obtain the AC solution under the assumption $\omega\varepsilon \ll \sigma$. Fields however need to satisfy the Helmholtz instead of Laplace equation, which will result in skin effects for sufficiently high frequencies. Solving for the fields everywhere and accounting for all the boundary conditions properly is possible but doing so only yields an error of up to 0.000042% in contact resistance when compared to the simplified solution (See appendix Appendix A where the full AC solutions are outlined).

With the assumption $\omega\varepsilon \ll \sigma$ on both channels, we may now construct the bulk resistance for the AC case, R_{b1} and R_{b2} in Eq. (2.4), as follows. First, for large values of $|z|$, the AC electric field has only a z-component which is uniform in z but nonuniform in y. It is shown in Appendix Appendix B that this bulk solution is given by (see Eqs. (5.5) and (5.7))

$$E_{z,1,b}(y) = \frac{I_0 \kappa_1}{2W\sigma_1} \frac{\cos(\kappa_1 y)}{\sin(\kappa_1 d_1)} \tag{2.5a}$$

$$E_{z,2,b}(y) = \frac{I_0 \kappa_2}{2W\sigma_2} \frac{\cos(\kappa_2 y)}{\sin(\kappa_2 d_2)} \tag{2.5b}$$

where

$$\kappa_1^2 = \mu_1 \varepsilon_1 \omega^2 + i\omega\mu_1\sigma_1 \simeq i\omega\mu_1\sigma_1 \equiv 2i/\delta_1^2 \tag{2.6a}$$

$$\kappa_2^2 = \mu_2 \varepsilon_2 \omega^2 + i\omega\mu_2\sigma_2 \simeq i\omega\mu_2\sigma_2 \equiv 2i/\delta_2^2 \tag{2.6b}$$

which includes the dominant skin effect, i.e., assuming $\sigma_{1,2} \gg \omega\varepsilon_{1,2}$. The skin depth for each material is:

$$\delta_1 = \sqrt{2/\sigma_1\mu_1\omega} \tag{2.7a}$$

$$\delta_2 = \sqrt{2/\sigma_2\mu_2\omega} \tag{2.7b}$$

Upon using the bulk field solution (2.5) into the integral (2.3) for each channel, we find the AC bulk resistance for each channel to be (see Eqs. (5.12) and (5.13) in Appendix Appendix B)

$$R_{b1} = \frac{L}{2W\sigma_1\delta_1} \frac{\sinh\left(\frac{2d_1}{\delta_1}\right) + \sin\left(\frac{2d_1}{\delta_1}\right)}{\cosh\left(\frac{2d_1}{\delta_1}\right) - \cos\left(\frac{2d_1}{\delta_1}\right)} \tag{2.8a}$$

$$R_{b2} = \frac{L}{2W\sigma_2\delta_2} \frac{\sinh\left(\frac{2d_2}{\delta_2}\right) + \sin\left(\frac{2d_2}{\delta_2}\right)}{\cosh\left(\frac{2d_2}{\delta_2}\right) - \cos\left(\frac{2d_2}{\delta_2}\right)} \tag{2.8b}$$

which is to be used in Eq. (2.4). Note that Eq. (2.8) reduces to the DC bulk resistance in Eq. (2.1) in the DC limit $\omega \to 0$, so that $\delta_1 \to \infty$ and $\delta_2 \to \infty$. At high frequencies, $\delta_1 \ll d_1$, and $\delta_2 \ll d_2$, Eq. (2.8) shows that the bulk resistances, R_{b1} and R_{b2}, increase with ω, like $\sqrt{\omega}$.

The total resistance, R, may then be obtained from Eq. (2.3) after solving for the AC field solution for the entire region, $-L < z < L$, and the contact resistance, R_c, may then be obtained by substituting Eq. (2.8) into Eq. (2.4). In the numerical examples given in Section 2.3, we will again represent this AC contact resistance,

$$R_c = \frac{\overline{R_c}}{4\pi W \sigma_2} \tag{2.9}$$

in terms of the normalized resistance $\overline{R_c}$, so that this AC value can immediately be compared with the DC value given in Eq. (2.1).

12

2.3 Numerical Examples of AC Contact Resistance

Numerical examples of the AC contact resistance are presented for three selected cases of Fig. 2.1: (A) $d_1 = d_2$, (B) $d_2 > d_1$, and (C) $d_2 - d_1 \ll d_1$ with $\sigma_1 = \sigma_2$. Case (A) shows the distinct nature of AC contact resistance, as the DC contact resistance equals zero in this case. It also reveals the surprising result that the contact resistance can be negative. Case (B) shows various scalings with frequencies, and Case (C) provides a closer examination of the frequency scaling, and offers a quantification of AC contact resistance for slightly uneven surfaces.

2.3.1 Case A: $d_1 = d_2 = d$
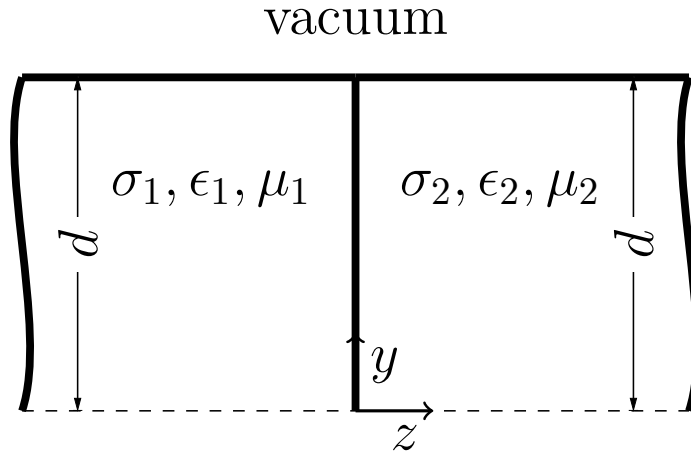
Figure 2.2: The setup for $d_1 = d_2 = d$.

The setup for this case is shown in Fig. 2.2. This case is trivial for the DC case in which the contact resistance is zero as the bulk fields are uniform and therefore the sum of the bulk resistance becomes the total resistance. For the AC case however, the bulk fields shown in equation (2.5) do not satisfy the appropriate boundary conditions for $\sigma_1 \neq \sigma_2$ because of the different skin depths in each material. Without loss of generality we will assume $\sigma_1 > \sigma_2$. By satisfying the boundary conditions on the interface z=0 we can obtain the normalized contact resistance as a function of frequency, shown in Fig. 2.3.
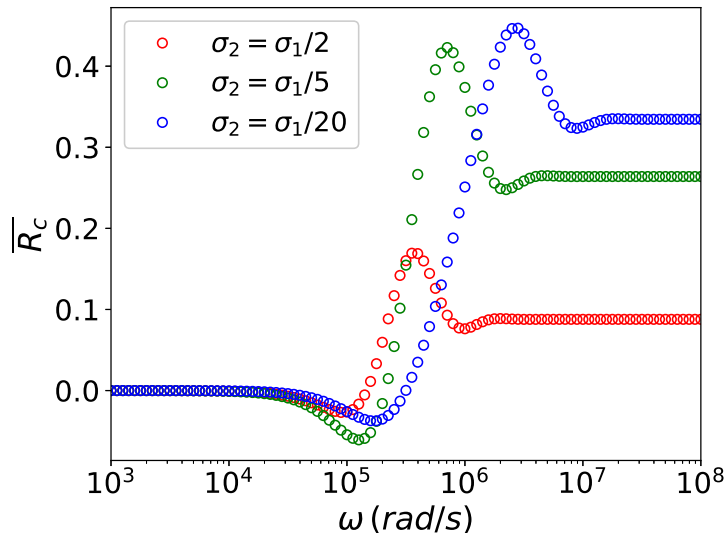
Figure 2.3: Normalized contact resistance vs frequency for $d_1 = d_2 = d = 1$ mm, $\sigma_1 = 3.69 \cdot 10^7$ S/m.

There are a few interesting features in Fig. 2.3. First, for low frequencies we obtain $\overline{R_c} = 0$. This is because at low frequencies the skin depth is large and therefore the fields are merely oscillating uniform fields. This was found to be true for $d/\delta_1 < 1$. For high frequencies we observe a constant contact resistance. This can be explained: at high frequencies both conductors demonstrate strong skin effects, and we may then take the small skin depths $\delta_{1,2}$ as the equivalent channel widths $d_{1,2}$ in a DC case and then use the scaling laws of the DC contact resistance to interpret the numerical results of the AC case. Note that the ratio of the skin depths is constant with frequency and that for the DC case, the contact resistance is only a function of d_2/d_1 [64]. Therefore, as we change the frequency, the skin depths also change but not their ratio, so the contact resistance is unchanged at high frequencies. This high-frequency constant contact resistance was observed for $d/\delta_2 > 4$. Note that the spreading resistance shown in Fig. 2.3 approaches a constant at high frequencies, whereas the bulk resistance increases with frequency according to Eq. (2.8); the relative effect of spreading resistance diminishes at high frequencies. (In a slightly different context, seen in [45], the spreading resistance also approaches a constant at high frequencies, whereas the bulk resistance increases with frequencies. Constriction resistance at very small skin depths were explored by Zhang, Lau, and Timsit [35, 36], and by Timsit [3].

For intermediate frequencies the contact resistance transitions between the two constant values at low and high frequencies. A further interesting behavior is observed at the lower end of this transition: we obtain $\overline{R_c} < 0$. (Fig. 2.3) This, of course, does not indicate an overall power gain, but a current distribution

14

that is less dissipating compared to the bulk currents. This can be seen in Fig. 2.4 which shows the current flow pattern when the AC contact resistance is negative (a), zero (b), and positive (c). Figure 2.4b shows zero AC contact resistance, meaning that the total AC resistance in the two conductors happen to be equal to the sum of their respective AC bulk resistance. Compared with Fig. 2.4b, Fig. 2.4c (2.4a) exhibit more (less) current crowding than Fig. 2.4b, and therefore its contact resistance is positive (negative) in comparison. That is, Fig. 2.4a (Fig. 2.4c) will produce less (more) electrical heating than that expected from the bulk current of the two conductors. We wish to remark that the seemingly unusual "negative contact resistance" is analogous to the "negative energy waves" encountered in plasma physics [77], in that they both arise in comparison with some reference state. For "negative energy waves", that reference state is the unperturbed state in a small signal theory.
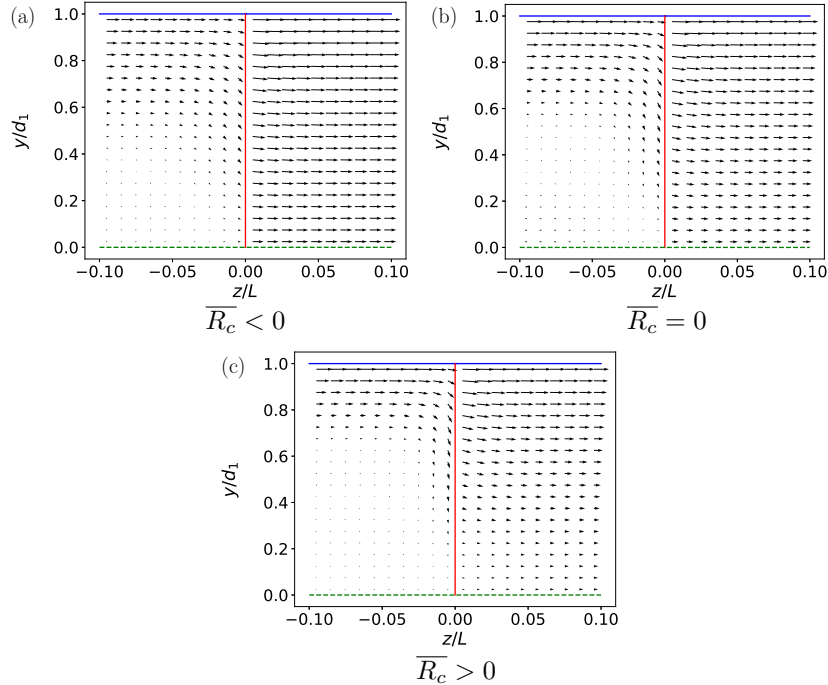
Figure 2.4: Current flow patterns for Fig. 2.2 which show (a) negative, ($\omega = 1.33 \cdot 10^5$ rad/s, $\overline{R_c} = -0.053$), (b) zero ($\omega = 2.66 \cdot 10^5$ rad/s, $\overline{R_c} = 0$), and (c) positive ($\omega = 5.32 \cdot 10^5$ rad/s, $\overline{R_c} = 0.228$) AC contact resistance. Here, $d_1 = d_2 = 1$ mm, $\sigma_1 = 10\sigma_2 = 3.69 \cdot 10^7$ S/m.

2.3.2 Case B: $d_1 < d_2$

This is the more general case. We can numerically solve the boundary conditions (2.2a-2.2e) assuming the bulk currents in (2.5) to obtain the remaining fields

in both conductors and use those remaining fields to find the normalized AC contact resistance by solving (2.3) and (2.4) using (2.8). Doing so we obtain $\overline{R_c}$ as a function of ω in Fig. 2.5.
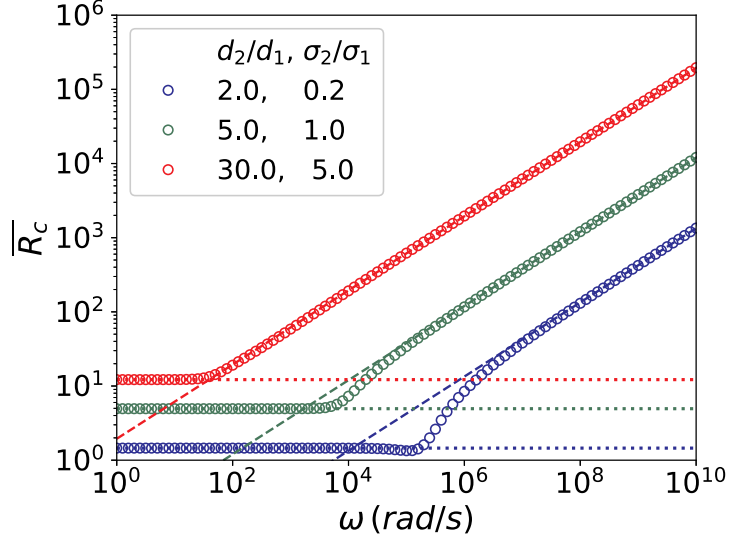
Figure 2.5: $\overline{R_c}$ vs ω for various parameters. For all cases $d_1 = 1mm$, $\sigma_1 = 3.69 \cdot 10^7$ S/m. Dotted lines represent the DC contact resistance for each case. Dashed lines represent Eq. (2.10) for each case.

There are three distinct regions in Fig. 2.5. For low frequencies the contact resistance is constant and equal to the DC contact resistance [64]. This is because the skin depths are large and the slowly oscillatory fields are basically the uniform DC fields. For high frequencies we observe $\overline{R_c} \propto \sqrt{\omega}$. To see this, we note that at high frequencies all currents will be limited to the surface of each conductor because of skin effects. The current profile will resemble Fig. 2.6. The currents along the top of each conductor are the bulk currents and will not contribute to the contact resistance. The current flowing between points K and M in Fig. 2.6 will be solely responsible for the dissipating losses that result in contact resistance. In Appendix Appendix C, Eq. (5.18), we show that, at very high frequencies,

$$\overline{R_c} = 2\pi \frac{d_2 - d_1}{\delta_2} \tag{2.10}$$

16
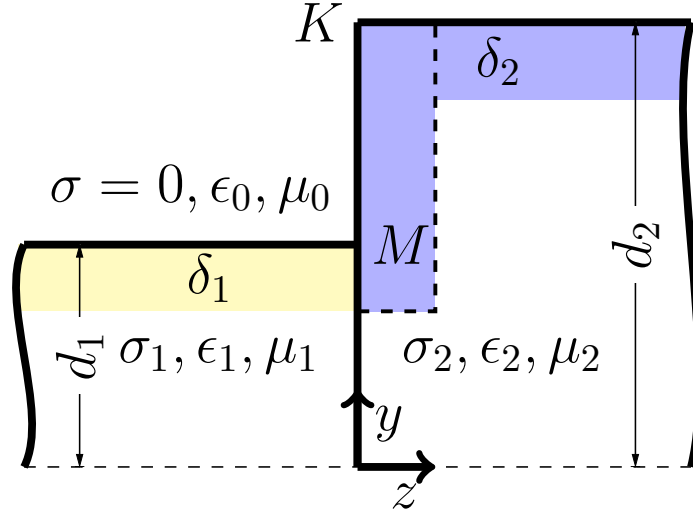
Figure 2.6: Schematic drawing of the current profile near the channel surface in each conductor for high frequencies.

Eq. 2.10 shows that $\overline{R_c} \propto \sqrt{\omega}$ at high frequencies. For intermediate frequencies the contact resistance transitions between the two asymptotes. (Fig. 2.5)

2.3.3   Case C: $d_2 - d_1 \ll d_1$, $\sigma_1 = \sigma_2 = \sigma$

This case represents a single conductive medium with an uneven joint, as seen in Fig. 2.7. It may also mimic some local surface roughness.
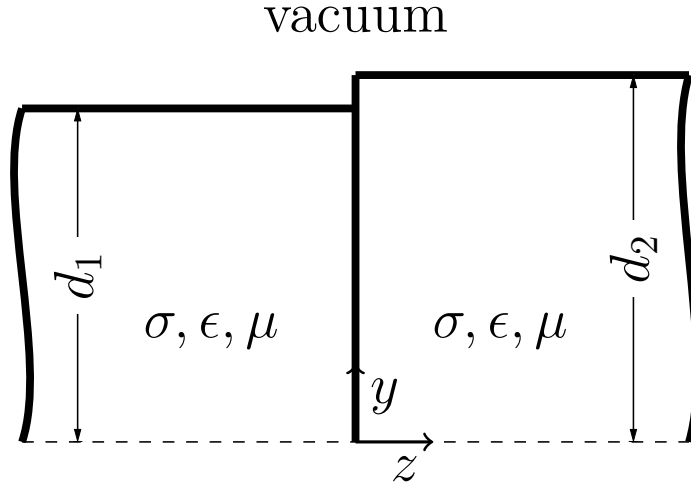
Figure 2.7: An uneven joint for a single material for case C, with $(d_2 - d_1) \ll d_1$.

As in case B we can solve for the fields and contact resistance as a function of frequency. Doing so we obtain $\overline{R_c}$ as a function of ω as shown in Fig. 2.8.
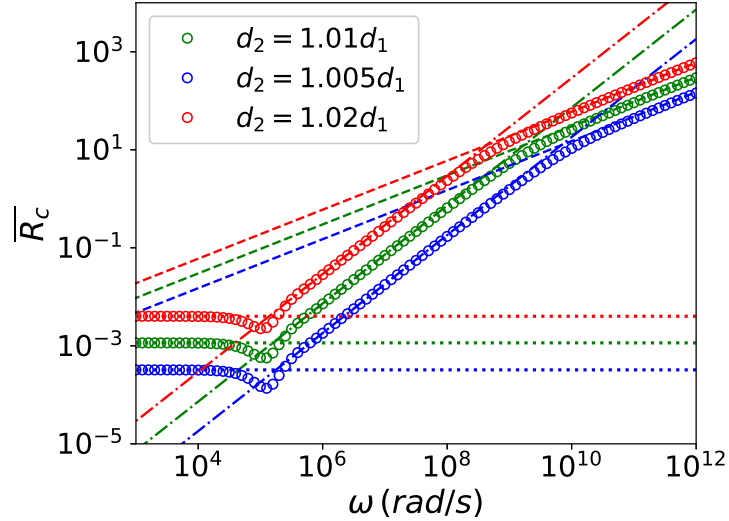
Figure 2.8: $\overline{R_c}$ vs ω for an uneven joint. The dotted line represents the DC value for contact resistance, while the dashed line represents Eq. (2.10). The dash-dotted line represents the fitted line $\overline{R_c} = 2.28 \left(\frac{d_2 - d_1}{\delta} \right)^2$. Here $d_1 = 1$ mm, and $\sigma_1 = 3.69 \cdot 10^7$ S/m.

At low frequencies we again obtain a constant value for $\overline{R_c}$ that is equal to the DC contact resistance as in cases A and B. For very high frequencies $(\delta \ll d_2 - d_1 \ll d_1)$ we obtain the frequency dependence described by (2.10), since the field profiles will look similar to those seen in Fig. 2.6. In this regime, the skin depth is much less than the "misalignment" or "roughness", $(d_2 - d_1)$. It is then not surprising that the constriction resistance may far exceed the DC value, even though this misalignment is only 0.5% of the current channel width. For intermediate frequencies $(d_2 - d_1 \ll \delta \ll d_1)$ we observe $\overline{R_c} \propto \omega$, from the numerical data (the dash-dotted curves in Fig. 2.8). So far, we were unable to derive this frequency scaling even though for these intermediate frequencies the current profile will look like Fig. 2.9. Note that the $\overline{R_c} \propto \omega$ scaling for the intermediate frequency regime is also suggested in the lower two curves in Fig. 2.5.
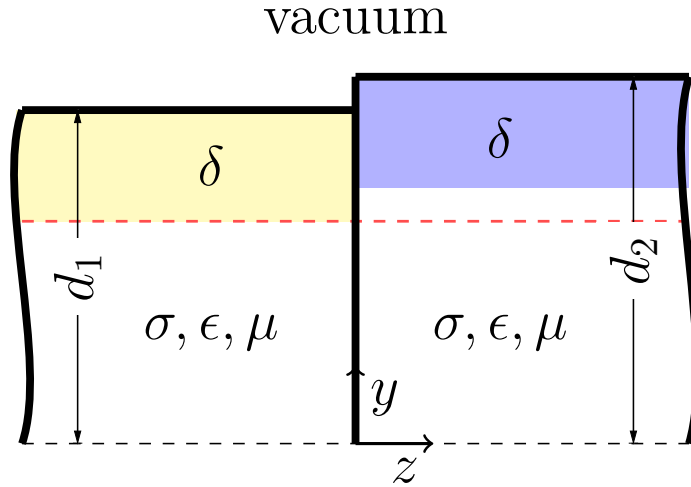
Figure 2.9: The current profiled for $d_2 - d_1 \ll \delta \ll d_1$.

2.4   Triple Point

One of the major difficulties when computing the fields is the triple point that occurs when the two conductors and vacuum all come in contact. The point $(y, z) = (d_1, 0)$ in Fig. 2.1 is one such point, which we shall examine in this section. Fields on this point diverge, which requires a high number of terms in our Fourier series to be considered. Specifically, when $\sigma_1 \gg \sigma_2$ the current tends to bunch close to the triple point causing solution convergence to be especially poor. This is observed for the DC case [64] as well for the AC case studied in this thesis. It is therefore desirable to obtain the nature of the divergence of the electric fields and subtract it out to obtain fields that converge everywhere. If this is done successfully, we should be able to obtain fields that converge better and faster.
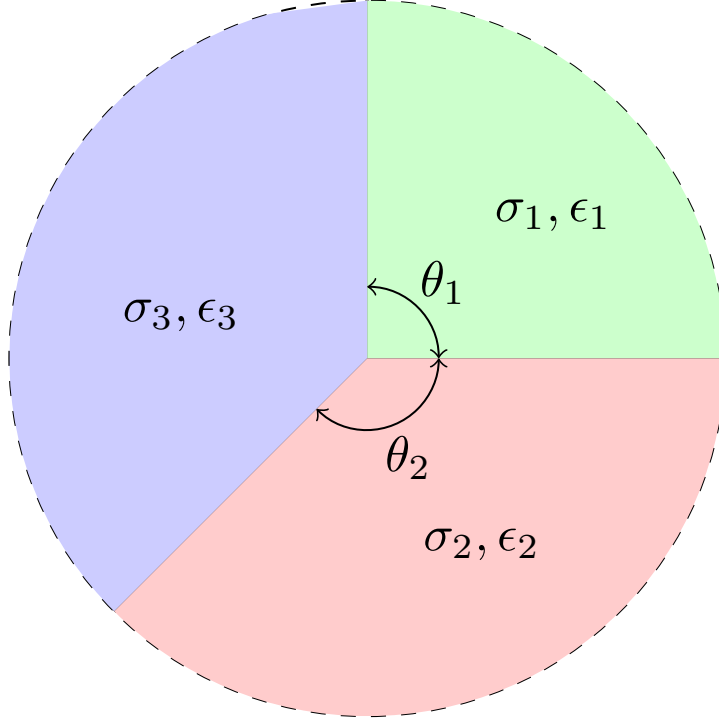
Figure 2.10: The configuration used to obtain the triple point fields.

For this purpose, we consider the general triple point in cylindrical coordinates shown in Fig. 2.10. Three materials that extend arbitrarily in z are all interfacing on the line $r = 0$. Each material has unique properties σ and ε, and occupies an angle θ with $\theta_1 + \theta_2 + \theta_3 = 2\pi$. All fields are assumed to have a $e^{-i\omega t}$ time dependence. Solving Maxwell's equations yields the following electric fields for each material, asymptotically (see Appendix Appendix D).

$$E_z \simeq \left(ae^{im\phi} + be^{-im\phi}\right) r^{m-1} \tag{2.11a}$$

$$E_z \simeq i\left(ae^{im\phi} - be^{-im\phi}\right) r^{m-1} \tag{2.11b}$$

Note that the above are exact solutions to the Maxwell's equations for $\omega = 0$. The triple point in this DC limit was treated by Jordan et al. [86]. For the boundary conditions to be satisfied across all three interfaces we need to have identical values for m in each of the three materials. The values of a and b in each material are unknowns. Furthermore, m is also unknown. We can use the fact that E_r and $(\sigma - i\omega\varepsilon)E_\phi$ must be continuous across each boundary to get a total of six equations. Assuming these equations have a non-trivial solution for the values of a and b we can obtain the value of m. This tells us how the fields diverge as $r \to 0$.

Going back to our problem the above can be used to obtain the nature of

20

divergence of solutions around the triple point. The value m as a function of the ratio of conductivities, σ_2/σ_1 for $\omega = 0$ is plotted in Fig. (2.11), which confirms that fields diverge at a more rapid pace for $\sigma_2 \gg \sigma_1$. Checking the convergence predicted by this theory against the solutions obtained in previous chapters we observe that indeed r^{m-1} is the divergence rate close to the triple point as expected.
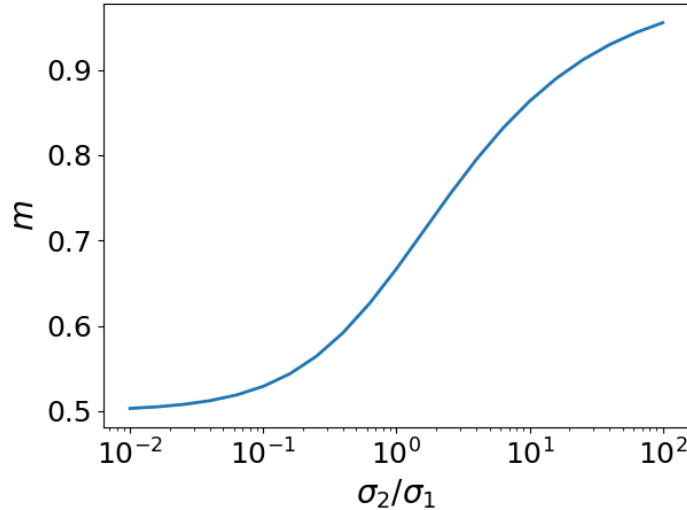
Figure 2.11: m as a function of σ_2/σ_1 for $\omega = 0$, for the triple point $(y, z) = (d_1, 0)$ in Fig. 2.1 with $d_2 = 3d_1$

Implementing the above to help solve our problem is another challenge. Doing so for the DC case is much easier for two reasons. First, as mentioned earlier, (2.11) is the exact solution to Maxwell's equations and so the triple point fields will satisfy boundary conditions for all r. Second, the exact triple point fields for the AC case are exponentially growing as r increases (see Appendix Appendix D). It is for these reasons that we were able to implement the triple point for the DC case but not as conveniently for the AC case. In Fig. 2.12 we see the solution obtained using our previous numerical method as well as the results obtained when using the triple point method. Note that the previous numerical method uses ten times more terms per series expansion and took about 400 times longer to compute, showing the potential improvements that implementing the triple point solutions can have. There are however drawbacks to this method as well. The resulting fields are expressed as a combination of functions in Cartesian and cylindrical coordinates and therefore the energy dissipation is harder to compute. Also, the triple point fields diverge exponentially as r increases in the AC case, so they can only be considered close to the triple point introducing additional boundaries. The AC triple point deserves further

21

analysis.
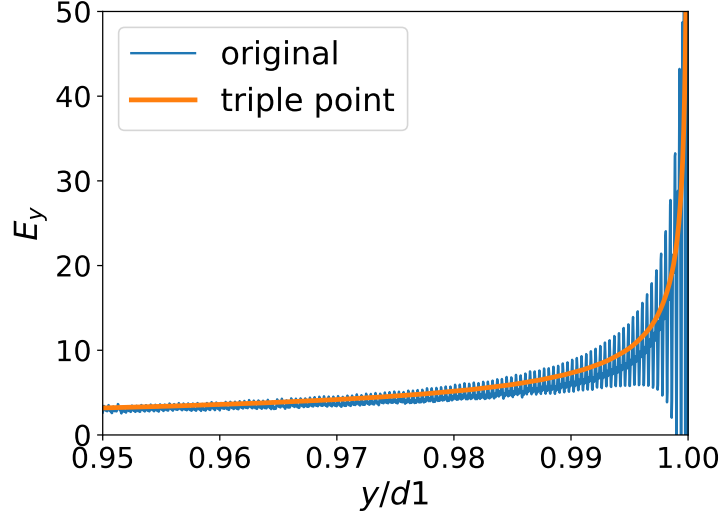
Figure 2.12: E_y as a function of y/d_1 in the DC limit for the triple point in Fig. 2.1 with $d_1 = 1$ mm, $d_2 = 3$ mm, $\sigma_1 = 3.69 \cdot 10^7$ S/m and $\sigma_2 = 3.69 \cdot 10^6$ S/m. The blue (original) calculation simply solves for the fields by matching all boundary conditions across each boundary, while the orange (triple point) calculation implements the triple point fields and only needs to solve for finite fields everywhere.

2.5 Low Frequency Capacitive Effects

This section gives a rudimentary consideration of the low frequency capacitive effects on contact resistance, via an example in field effect transistor. When transitioning from DC to low frequency electromagnetic fields begin to oscillate without any skin effects being present. When considering an interface between two materials with imperfect contact there will be enhanced heating that occurs because of the current crowding to pass through the physical contacts, which can characterized by contact resistivity ρ_c, in $\Omega \cdot m^2$. The gaps present between the two materials can act as capacitors, whose capacitance can be calculated as:

$$C = p\varepsilon_0 \frac{A}{d} \tag{2.12}$$

where p is the fraction of the interface that consists of gaps, A is the area of the interface and d is the average gap distance. This capacitance will act in parallel to the contact resistance, which will decrease the effective impedance of the contact under AC.

$$Z = \frac{1}{\frac{1}{R_c} - i\omega C} \tag{2.13}$$

Combining Eq. (2.12) and (2.13) we obtain the modified AC contact resistivity, from its DC value ρ_c:

$$\rho_{c,AC} = \text{Re}(Z)A = \frac{\rho_c}{1 + \left(\frac{\rho_c \varepsilon_0 p \omega}{d}\right)^2} \tag{2.14}$$

This can be used in conjunction with known contact resistivities to obtain the modified AC contact resistivity. As an example in field effect transistor [87], consider the resistance of FinFETs which typically operated in the $1-10$ GHz range. Using the contact resistivity [87] reported $\rho_c = 2$ n$\Omega \cdot$ cm^2, $p = 0.5$ assuming half the interface consists of gaps and $d = (l_{Cu} + l_{Si})/2$ where $l_{Cu} = 265$ pm is the nearest atom distance of Copper and $l_{Si} = 235$ pm is the nearest atom distance of Silicon. We obtain the modified AC contact resistivity as a function of frequency, seen in Fig. 2.13. The reduction of the AC contact resistivity at high frequencies shown in Fig. 2.13 is due to the increase in the displacement current in providing current transport across the contact. The displacement current density ($-i\omega\epsilon_0 \boldsymbol{E}$) is always 90 degrees out of phase with the local electric field $\boldsymbol{E}$ and, therefore, it does not dissipate any ohmic power.
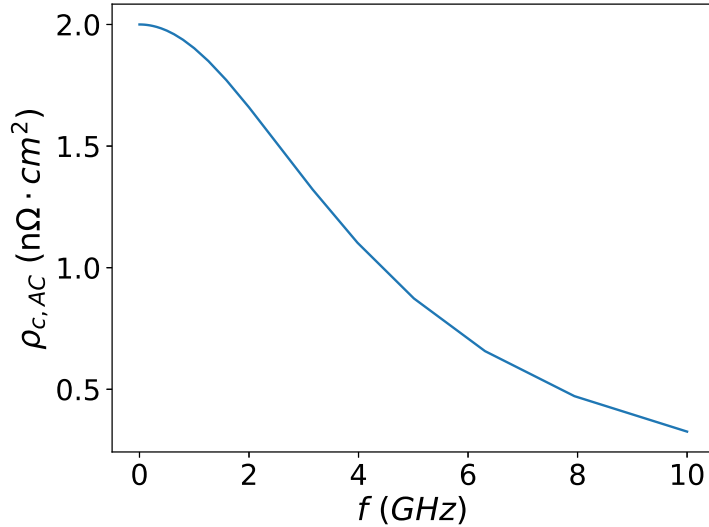
Figure 2.13: Predicted modified AC contact resistivity as a function of frequency for the parameters found in [87].

2.6 Concluding Remarks

In this chapter, we analyze the contact resistance in two Cartesian current channels of dissimilar materials and different widths, under the AC condition as shown in Fig. 2.1. Because of skin effects even the bulk current densities are different from the DC case, leading to different expressions for the bulk

resistances (Eq. (2.8)) than for the DC case (Eq. (2.1)). Assuming $\sigma \gg \varepsilon\omega$ we can ignore currents flowing into conductor-vacuum interfaces, thereby simplifying the problem considerably. Three different cases were studied to obtain scaling laws for contact resistance as a function of frequency. For equal channel widths, $d_1 = d_2$, the low frequency limit always yields a zero contact resistance, which rises to a nonzero, constant value when the frequency is increased to a sufficiently high level. In this transition, negative contact resistance was observed, and interpreted as the total resistance shown in Fig. 2.1 being less than the total bulk resistance of the individual channels. In the general case where $d_1 \neq d_2$, we obtain the DC contact resistance at low frequencies but find the normalized contact resistance $\overline{R_c} \propto \omega^{1/2}$ at very high frequencies. For a slightly uneven joint, $d_2 - d_1 \ll d_1$, $\sigma_1 = \sigma_2$ we obtain the DC contact resistance at low frequencies, $\overline{R_c} \propto \omega$ at intermediate frequencies, and $\overline{R_c} \propto \omega^{1/2}$ at high frequencies. The contact resistance is significantly more difficult to compute if we relax the assumption $\sigma \gg \varepsilon\omega$.

When we are able to unambiguously define the AC contact resistance, by considering the ohmic power loss, the derived contact resistance may then be considered as a lumped circuit parameter. As of this writing, we were unable to find suitable and unambiguous definitions for the other lumped circuit parameters, the inductance and capacitance, for the current channel shown in Fig. 2.1, even under the assumption $\sigma \gg \varepsilon\omega$.

In Fig. 2.1, the point $(y, z) = (d_1, 0)$ is a "triple point", the intersection of two different materials with vacuum [86]. We have examined in some details the AC solutions at this triple point. This problem is of practical and computational interest, but is worth a future investigation.

Once more, if the conductivity σ is so small (like a semiconductor) or ω is so high (like submillimeter waves) that the simplifying assumption $\sigma \gg \varepsilon\omega$ is no longer valid, the contact resistance calculation will become very difficult. For one thing, the radiative loss, which is negligible in this chapter, may need to be accounted for in the consideration of total power balance.

Chapter 3. Effects of Temperature Dependence of Electrical and Thermal Conductivities on the Joule Heating of a One Dimensional Conductor

In this chapter, we evaluate the effects of temperature dependence of the electrical and thermal conductivities on the Joule heating of a one-dimensional conductor, by solving the coupled non-linear steady state electrical and thermal conduction equations. Section 3.1 provides the formulation of our simple theory. Results and discussions are given in Section 3.2, where we have analyzed four cases: 1) a constant electrical conductivity paired with a thermal conductivity that depends linearly on temperature, 2) linear temperature dependence of both electrical and thermal conductivities, 3) the Wiedemann–Franz law, and 4) realistic examples for carbon nanotube fibers and copper. A comparison of this theory and experiments is given in Section 3.3. A summary and suggestions for future research are given in Section 3.4.

3.1   Formulation

Consider a one-dimensional (1D) conductor of length L, which is held at temperatures T_1 and T_2 at its ends, and across which a voltage of V_0 is applied. Without loss of generality we assume $T_1 \leq T_2$. The steady state heat conduction and electrical current continuity equations are, respectively,

$$\frac{d}{dz}\left(\kappa(T)\frac{d}{dz}T(z)\right) + \sigma(T)\left(\frac{d}{dz}V(z)\right)^2 = 0 \tag{3.1}$$

$$\frac{d}{dz}\left(\sigma(T)\frac{d}{dz}V(z)\right) = 0 \tag{3.2}$$

where $\kappa(T)$ and $\sigma(T)$ are the temperature-dependent thermal and electrical conductivity, respectively, and V(z) is the potential, T(z) is the temperature and z is the location along the 1D conductor. Eq. (3.1) is the 1D version of the heat conduction equation $\nabla \cdot (\kappa \nabla T) = -\boldsymbol{J} \cdot \boldsymbol{E}$ and Eq. (3.2) is the continuity equation $\nabla \cdot \boldsymbol{J} = 0$, where $\boldsymbol{J} = \sigma \boldsymbol{E} = -\sigma \nabla V$ has been used. Equations (3.1) and (3.2) are solved with the following boundary conditions,

$$T(z = 0) = T_1 \tag{3.3a}$$
$$T(z = L) = T_2 \tag{3.3b}$$
$$\phi(z = 0) = 0 \tag{3.3c}$$
$$\phi(z = L) = V_0 \tag{3.3d}$$

Combining Eqs. (3.1), (3.2), (3.3c) and (3.3d), we have

$$\frac{d}{dz}\left(\kappa(T)\frac{dT}{dz}\right) + \frac{J_c^2}{\sigma(T)} = 0 \tag{3.4}$$

where $J_c = \sigma dV/dz =$ constant is the current density in the conductor, which satisfies $\int_0^L (J_c/\sigma)\, dz = V_0$.

For simplicity, we introduce the normalizations, $\overline{z} = z/L$, $\overline{T} = (T - T_1)/T_0$, with $T_0 = T_1$ if $T_1 = T_2$, and $T_0 = T_2 - T_1$ if $T_1 \neq T_2$, $\overline{V} = V/V_0$, $\overline{\kappa}(\overline{T}) = \kappa(T)/\kappa_0$, $\overline{\sigma}(\overline{T}) = \sigma(T)/\sigma_0$, $\alpha = \sigma_0 V_0^2/\kappa_0 T_0$, $J_0 = \sigma_0 V_0/L$, and $\overline{J_c} = J_c/J_0$. κ_0 and σ_0 are constants to be defined individually below in Section 3.2, where we treat different models. Equation (3.4) becomes

$$\frac{d}{d\overline{z}}\left(\overline{\kappa}\frac{d\overline{T}}{d\overline{z}}\right) = -\alpha\frac{\overline{J_c}^2}{\overline{\sigma}} \qquad (3.5)$$

where $\overline{J_c}\int_0^1 d\overline{z}/\overline{\sigma} = 1$, and the boundary conditions (Eqs. 3.3a and 3.3b) are,

$$\overline{T}(\overline{z} = 0) = 0 \qquad (3.6a)$$

$$\overline{T}(\overline{z} = 1) = \begin{cases} 0, & \text{if } T_1 = T_2 \\ 1, & \text{if } T_1 \neq T_2 \end{cases} \qquad (3.6b)$$

Equations (3.5) and (3.6) are solved to give the steady-state solution for the coupled electrical-thermal conduction. In principle, they can be solved numerically for arbitrary temperature dependence of electrical conductivity $\overline{\sigma}(\overline{T})$ and thermal conductivity $\overline{\kappa}(\overline{T})$. However, the parametric dependencies of the solution are difficult to determine from such purely numerical calculations. Thus, we focus on several special cases that can be of practical importance.

3.2 Results and Discussion

We consider four (4) cases in this section. (1) σ is a constant and κ is a linear function of T. (2) Both σ and κ are linear functions of T. (3) σ and κ are governed by the Wiedemann-Franz law. (4) σ and κ are taken from empirical data of carbon nanotube experiments.

3.2.1 Case 1: Constant electrical conductivity, and linear temperature dependent thermal conductivity

For the special case of constant electrical conductivity, $\sigma = \sigma_0$, and linear temperature dependence of thermal conductivity, $\kappa = \kappa_0 + \kappa'(T - T_1)$, we have $\overline{\sigma} = 1$, and $\overline{\kappa} = 1 + \eta\overline{T}$, with $\eta = \kappa'T_0/\kappa_0$. This case can be solved analytically from Eqs. (3.5) and (3.6), which gives

$$\overline{T}(\overline{z}) = \frac{-1 + \sqrt{\alpha\eta\overline{z}(1 - \overline{z}) + 1}}{\eta}, \qquad \text{if } T_1 = T_2 \qquad (3.7a)$$

$$\overline{T}(\overline{z}) = \frac{-1 + \sqrt{-\eta\alpha\overline{z}^2 + \eta(\alpha + \eta + 2)\overline{z} + 1}}{\eta}, \qquad \text{if } T_1 \neq T_2 \qquad (3.7b)$$

For the case of $T_1 = T_2$ the temperature distribution along the 1D conductor from Eq. (3.7) is plotted in Fig. 3.1a, for various values of α and η. The maximum temperature $\overline{T_{max}}$ is

$$\overline{T_{max}} = \frac{-1 + \sqrt{\alpha\eta/4 + 1}}{\eta}, \quad \text{if } T_1 = T_2 \tag{3.8}$$

which always occurs at the center of the 1D conductor $\overline{z_{max}} = 0.5$, as seen in Fig. 3.1a. However, it is important to note that the solution in Eq. (3.7a) becomes unphysical when $\alpha\eta < -4$. This happens when $\overline{T}$ becomes such that $\kappa \leq 0$ at some location (e.g. $\overline{z_{max}}$) of the 1D conductor. We note that the absence of a steady state solution may or may not indicate thermal runaway [88].
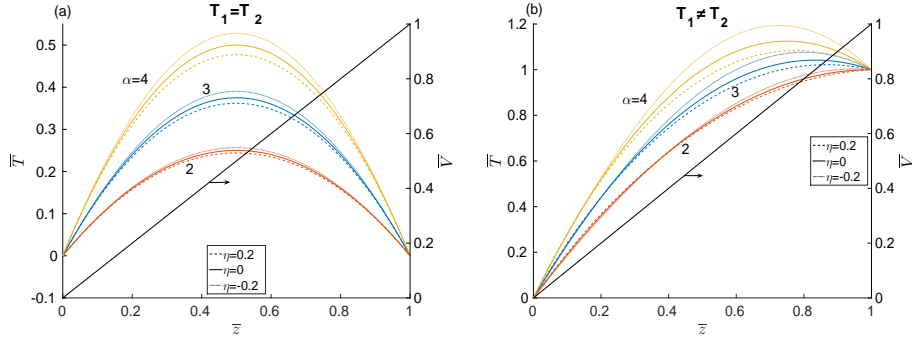
Figure 3.1: Steady state solution $\overline{T}(\overline{z})$ for (a) $T_1 = T_2$ from Eq. (3.7a) and (b) $T_1 \neq T_2$ from Eq. (3.7b) for various values of α and η.

For the case of $T_1 \neq T_2$, the temperature distribution along the 1D conductor from Eq. (3.7b) is plotted in Fig. 3.1b, for various values of α and η. When $T_1 \neq T_2$, the maximum temperature is found from Eq. (3.7b) to be,

$$\overline{T_{max}} = \begin{cases} \frac{-1 + \sqrt{\eta(\alpha + \eta + 2)^2/(4\alpha) + 1}}{\eta}, & \text{if } \eta + 2 < |\alpha| \text{ and } T_1 \neq T_2 \\ 1, & \text{if } \eta + 2 \geq |\alpha| \text{ and } T_1 < T_2 \end{cases} \tag{3.9}$$

which occurs at $\overline{z_{max}} = (\alpha + \eta + 2)/\alpha$ when $\alpha(\eta + 2) < \alpha^2$, and at $\overline{z_{max}} = 1$ otherwise. In the last case, the temperature range along the 1D conductor is bounded by the temperature at two ends, $[T_1, T_2]$.

For $T_1 \neq T_2$, the conditions for the existence of physical steady-state solution in Eq. (3.7b) are

$$a \leq -\frac{(\eta + 2)^2}{\eta}, \qquad \text{if } -1 \leq \eta < 0 \tag{3.10}$$

$$a \geq -\frac{(\eta + 2)^2}{\eta}, \qquad \text{if } \eta > 0 \tag{3.11}$$

27

These conditions are plotted in Fig. 3.2; within the bounds shown it is ensured that $\kappa > 0$ for all points along the 1D conductor. Note that in the limit of $\eta \to 0$, the RHS of Eq. (3.11) becomes $-(\eta + 2)^2/\eta \to -4/\eta$, which is the bound for the case of $T_1 = T_2$ (2nd sentence after Eq. (3.8)). This is expected since $\eta \to 0$ indicates $T_0 = T_2 - T_1 \to 0$, thus the solution asymptotically approaches that of $T_1 = T_2$. In the opposite limit of $\eta \to \infty$, $-(\eta + 2)^2/\eta \to -\eta$, the bound approaches $\alpha \geq -\eta$ asymptotically.

Note that as long as the electrical conductivity is a constant, $\bar{\sigma} = 1$, the current $\overline{J_c} = 1$ is independent of the temperature in the conductor.
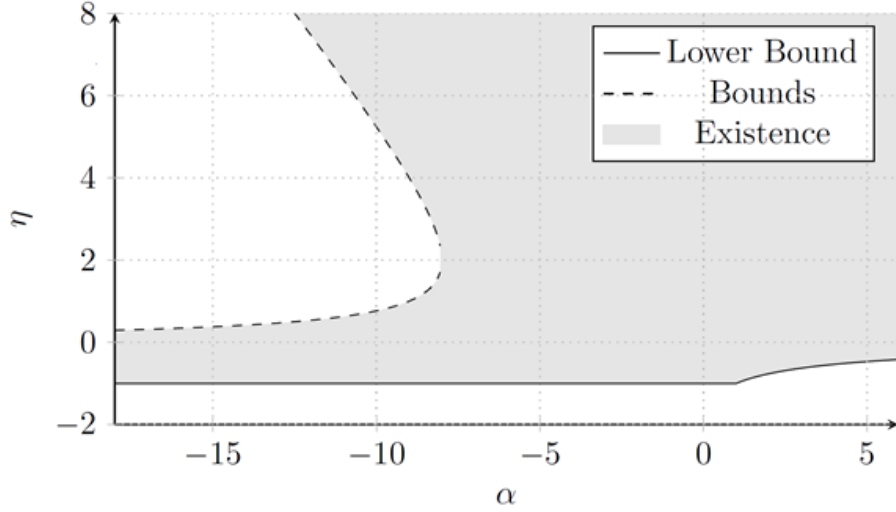
Figure 3.2: Bounds for the existence of steady-state solution for case 1 with $T_1 \neq T_2$.

3.2.2 Case 2: Linear temperature dependent of both electrical and thermal conductivities

In this case, we assume both electrical and thermal conductivities have linear temperature dependence,$\sigma = \sigma_0 + \sigma'(T - T_1)$ and $\kappa = \kappa_0 + \kappa'(T - T_1)$. After normalization, we have $\bar{\sigma} = 1 + \xi\overline{T}$, and $\bar{\kappa} = 1 + \eta\overline{T}$, with $\xi = \sigma'T_0/\sigma_0$, and $\eta = \kappa'T_0/\kappa_0$. Since analytical treatments are no longer available, Eqs. (3.5) and (3.6) are solved numerically.

As in Case 1, there exist bounds beyond which there is no steady state solution for Eqs. (3.5) and (3.6). These bounds are found numerically by scanning α and η for a given ξ. The results are shown in Fig. 3.3 for different values of ξ, for both $T_1 = T_2$ and $T_1 \neq T_2$. Note that now solutions do not exist when either $\kappa < 0$ or $\sigma < 0$. However, we limit the range of our numerical calculation to only track down the lack of solutions because of $\kappa < 0$ only, in order to compare the shifts of the bounds with respect to those in Case 1. As seen in Fig. 3.3, the lower bounds experience an upper left (lower right) shift

for increasing (decreasing) value of ξ for both $T_1 = T_2$ and $T_1 \neq T_2$, whereas the upper bounds (which only exist for the case $T_1 \neq T_2$) experience an upper right shift. That is, all the bounds shift towards $\alpha = 0$ as ξ increases. As we shall see later (Fig. 3.5), increasing ξ will increase the maximum temperatures in the conductor, thus $|\alpha|$ has to be reduced in order to decrease the rate of Joule heating (see Eq. (3.5)) to ensure existence of a steady state solution. Note that the bounds for $\xi = 0$ in Fig. 3.3b are identical to those in Fig. 3.2.
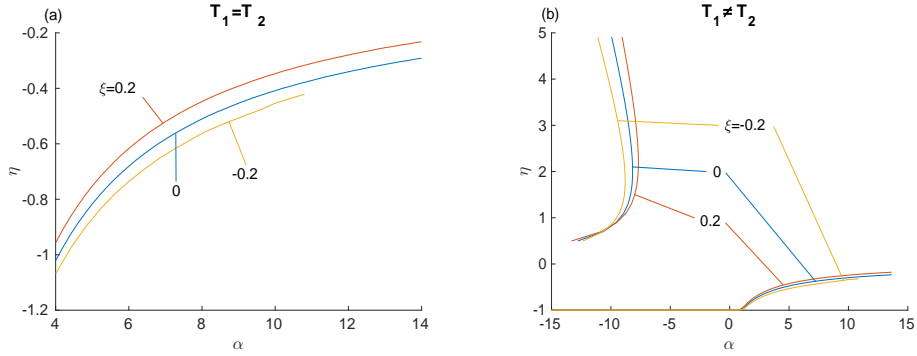
Figure 3.3: Bounds for the existence of steady-state solution for case 2 with (a) $T_1 = T_2$, and with (b) $T_1 \neq T_2$, for various values of ξ.

The temperature distribution along the 1D conductor calculated from Eqs. (3.5) and (3.6) is shown in Figs. 3.4a and 3.4b, for various values of α and ξ with $\eta = 0$. As ξ increases, the maximum temperature increases. For $T_1 = T_2$, the maximum temperature always occurs at the center of the conductor $\overline{z} = 0.5$. For $T_1 \neq T_2$, the position where maximum temperature occurs shifts towards $\overline{z} = 0.5$ as ξ increases. (See Fig. 3.5 and 3.6 for further details on these quantities.) The current $\overline{J_c}$ is plotted as a function of ξ, for various values of α in Figs. 3.4c and 3.4d. The value of $\overline{J_c}$ increases with ξ. For $\xi > 0$, $\overline{J_c}$ increases as α increases, whereas for $\xi < 0$, $\overline{J_c}$ decreases as α increases.

29
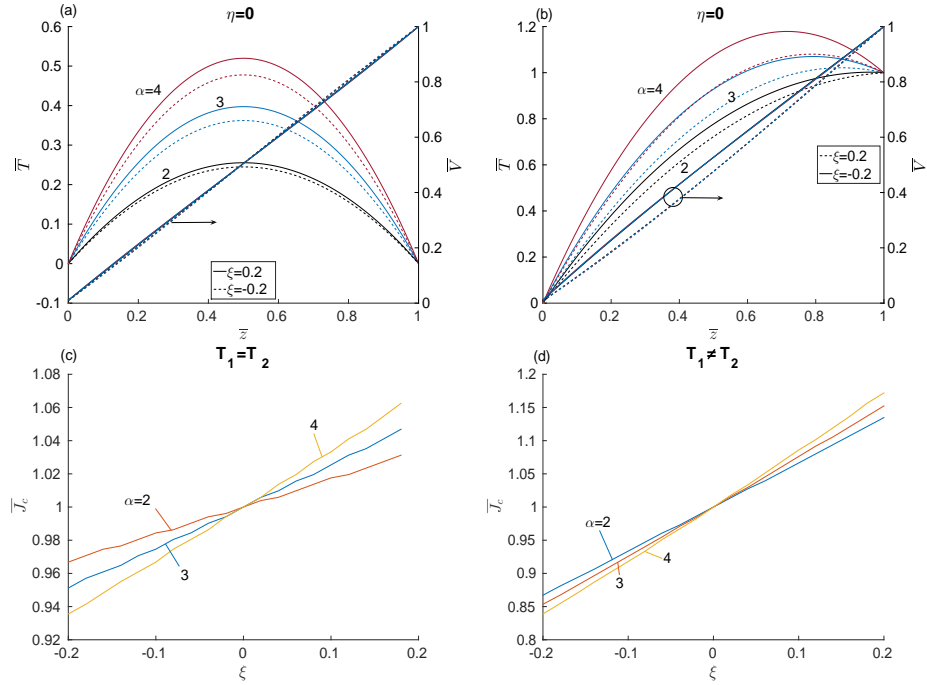
Figure 3.4: Steady state solution $\overline{T}(\overline{z})$ obtained from Eqs. (3.5) and (3.6) for (a) $T_1 = T_2$, and (b) $T_1 \neq T_2$, for various values of α and ξ for $\eta = 0$. The corresponding current $\overline{J_c}$ as a function of ξ for (c) $T_1 = T_2$, and (d) $T_1 \neq T_2$.
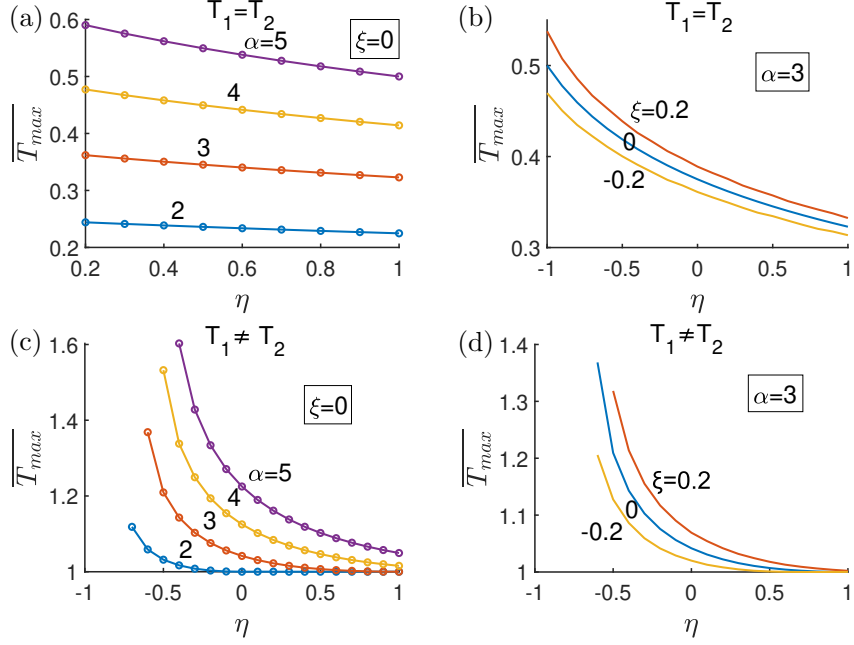
Figure 3.5: Maximum temperature $\overline{T_{max}}$ for various values of α and $\xi = 0$ (left) and for various values of ξ and $\alpha = 3$ (right). Both the cases $T_1 = T_2$ (top) and $T_1 \neq T_2$ (bottom) were plotted. The lines in (a) and (c) are from Eqs. (3.8) and (3.9), respectively.

The maximum temperature $\overline{T_{max}}$ is calculated numerically for different values of α, η, and ξ, as shown in Fig. 3.5. In all cases we can see that T_{max} decreases as η increases, this is because the increasing thermal conductivity $\overline{\kappa}$ will make the generated heat conducted away more easily. T_{max} increases as α increases, since the rate of heating increases with α (see Eq. (3.5)). It is also clear that T_{max} increases as ξ increases, since the current (thus the power) will increase in the conductor because of larger electrical conductivity $\overline{\sigma}$, at a fixed applied voltage V_0. Note that for the special case of $\xi = 0$, the numerical calculations in Figs. 3.5a and 3.5c give almost identical results obtained analytically from Eqs. (3.8) and (3.9).

For $T_1 = T_2$, the maximum temperature always occurs at $\overline{z_{max}} = 0.5$, because of symmetry. For $T_1 \neq T_2$ we plot $\overline{z_{max}}$ vs η in Fig. 3.6. It is apparent that $\overline{z_{max}}$ is located in the region of $0 \leq \overline{z_{max}} < 0.5$ when $\alpha < 0$ (i.e. $T_1 > T_2$), and within $0.5 < \overline{z_{max}} \leq 1$ when $\alpha > 0$ (i.e. $T_1 < T_2$). $\overline{z_{max}}$ becomes closer to 0.5 (the center) as $|\alpha|$ increases. Also, $\overline{z_{max}}$ becomes closer to 0.5 when either η decreases, or ξ increases. For the special case $\xi = 0$, the numerically obtained $\overline{z_{max}}$ give almost identical results from the analytical solution, where $\overline{z_{max}}(\neq 0, 1)$ is a linear function of η.
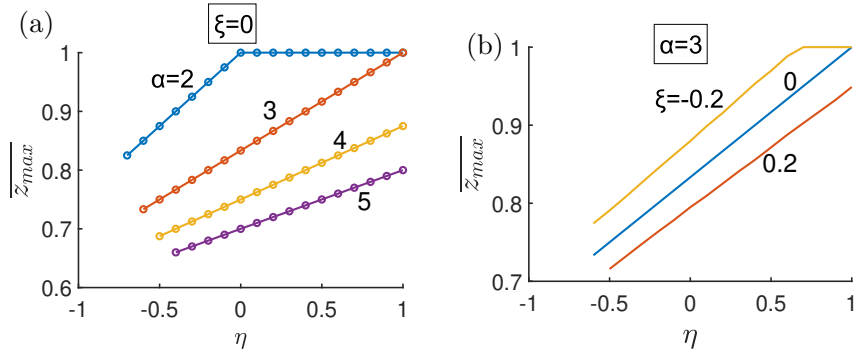
Figure 3.6: Location of maximum temperature for various values of α and $\xi = 0$ (left) and for various values of ξ and $\alpha = 3$ (right) for $T_1 \neq T_2$. The lines in (a) are from analytical calculation.

3.2.3 Case 3: Wiedemann–Franz law

The Wiedemann–Franz (WF) law [89, 90] is a relation between the thermal and electrical conductivity of metals of the form

$$\frac{\kappa}{\sigma} = lT \tag{3.12}$$

where $l \approx .44 \times 10^{-8}\, W\Omega K^{-2}$ is the Lorenz number. The Wiedmann-Franz law holds for metal conductors when free electrons are responsible for current flow. In such conductors κ is proportional to the average electron speed, $\overline{v}$ as temperature is dissipated mostly through electron collisions. Additionally σ is inversely proportional to $\overline{v}$ since electrons collisions slow electrons down and therefore limit the current. This implies $\kappa/\sigma \propto \overline{v}^2 \propto T$. For simplicity, we consider only the special case of $T_1 = T_2$ with linear temperature dependence of electrical conductivity, $\sigma = 1 + \xi\overline{T}$ (This does not contradict the previous claim that $\sigma \propto \overline{v} \propto \sqrt{T}$ for small temperature ranges where $\sqrt{T} \simeq \sqrt{T_0}(1 + (T - T_0)/2T_0)$). Using the same normalization as in Section 3.1, Eq. (3.12) becomes,

$$\overline{\kappa} = (1 + \overline{T})\overline{\sigma} \tag{3.13}$$

where we have used $\kappa_0/\sigma_0 = lT_1$ and the normalization $\overline{T} = (T - T_1)/T_1$, with $\alpha = V_0^2/lT_1^2$. Using Eq. (3.13), Eqs. (3.5) and (3.6) may be solved numerically. The temperature distribution is shown in Fig. 3.7a, for various values of α and ξ. It is notable that changes the value of ξ does not change the temperature profile significantly or the maximum temperature. The constant current $\overline{J_c}$ is plotted as a function of ξ, for various values of α in Fig. 3.7b. The behavior of $\overline{J_c}$ is similar to Case 2 with linear temperature dependence of σ and κ, as σ is modeled the same way and the temperature profile does not vary significantly.

Fig. 8 shows the maximum temperature does not depend on ξ but only on α. If the WF law holds, it is possible to find an analytical solution for the

maximum temperature (See Appendix Appendix E),

$$\overline{T_{max}} = \sqrt{1 + \frac{\alpha}{4}} - 1 \tag{3.14}$$

which is independent of $\overline{\sigma}(\overline{T})$ and $\overline{\kappa}(\overline{T})$, confirming our numerical data in Fig. 3.8.
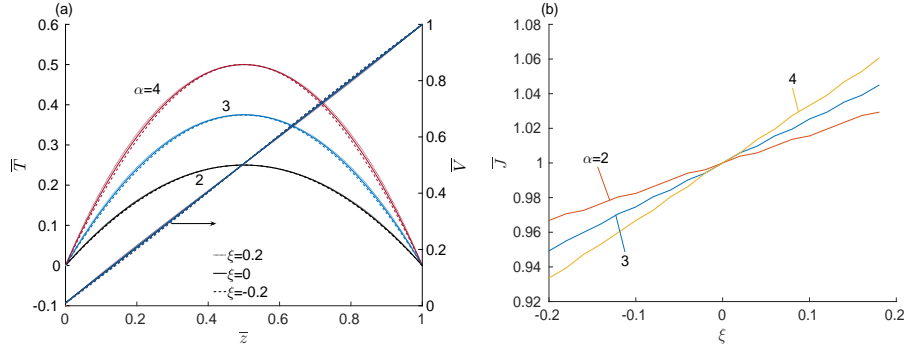
Figure 3.7: Steady state solution (a) $\overline{T}(\overline{z})$, and (b) $\overline{J_c}$ obtained from Eqs. (3.5) and (3.6) for $T_1 = T_2$ with the Wiedmann-Franz law assumed.
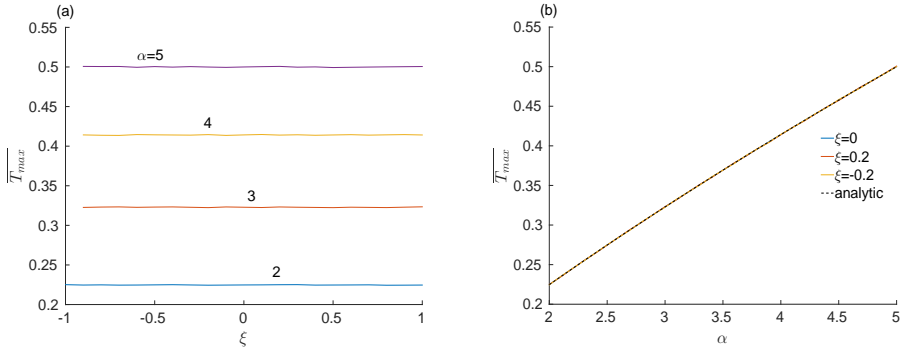
Figure 3.8: The maximum temperature (a) as a function of ξ for various values of α; (b) as a function of α for various values of ξ. Solid lines are for numerical calculation from Eqs. (3.5) and (3.6), dashed line is for analytical solution, Eq. (3.14).

3.2.4 Case 4: Realistic experimental data for carbon nanotube fibers and copper

We apply our theory to two examples, carbon nanotube fibers (CNFs) and copper, with realistic temperature dependent electrical conductivity $\sigma(T)$ and thermal conductivity $\kappa(T)$ taken from experimental measurements. For CNFs,

we use $\sigma(T)$ and $\kappa(T)$ from Fig. 3 of [12](samples A, B, and C). The data is polynomial interpolated, as shown in Figs. 3.9a and 3.9b. We then solve Eqs. (3.5) and (3.6) numerically. We assume the length of the CNFs is $L = 1$ μm. First, for $T_1 = T_2 = 360$ K, we calculate the maximum temperature T_{max} as a function of the applied voltage V_0, as shown in Fig. 3.9c. We next calculate T_{max} for various T_2, for a fixed bias voltage of $V_0 = 0.63$ V and $T_1 = 360$ K, as shown in Fig. 3.9d. The results are compared with those obtained for constant electrical and thermal conductivities, $\sigma(T) = \sigma_0 = \sigma(T = 360$ K), and $\kappa(T) = \kappa_0 = \kappa(T = 360$ K). The constant σ and κ approximation is fairly close to the actual data, for samples B and C, but not for sample A. This is because both electrical and thermal conductivities are close to constant for cases B and C in Figs. 3.9a and 3.9b. For sample A, σ increases and κ decreases with temperature T. As a result, the rate of Joule heating would increase faster than that of thermal conduction, resulting in a larger T_{max} in the conductor than that with constant conductivities. Noticeably, among the three samples, sample A had the weakest nanotube fiber alignment, the least emission current, the largest turn on voltage for field emission, and the smallest field enhancement factor [12].

For copper, we assume that the WF law holds. As discussed in Case 3 above, T_{max} can be found without knowing the detailed temperature of $\sigma(T)$ and $\kappa(T)$. For $T_1 = T_2 = 300$ K, the temperature of the electrical conductivity of copper [91] gives $\xi = -0.58$. Figure 3.10a shows the resulting maximum temperature T_{max} as a function of the applied voltage V_0, for $T_1 = T_2 = 300$ K. Figure 3.10b shows T_{max} as a function of T_2, for a fixed bias voltage of $V_0 = 0.63$ V and $T_1 = 300$ K.
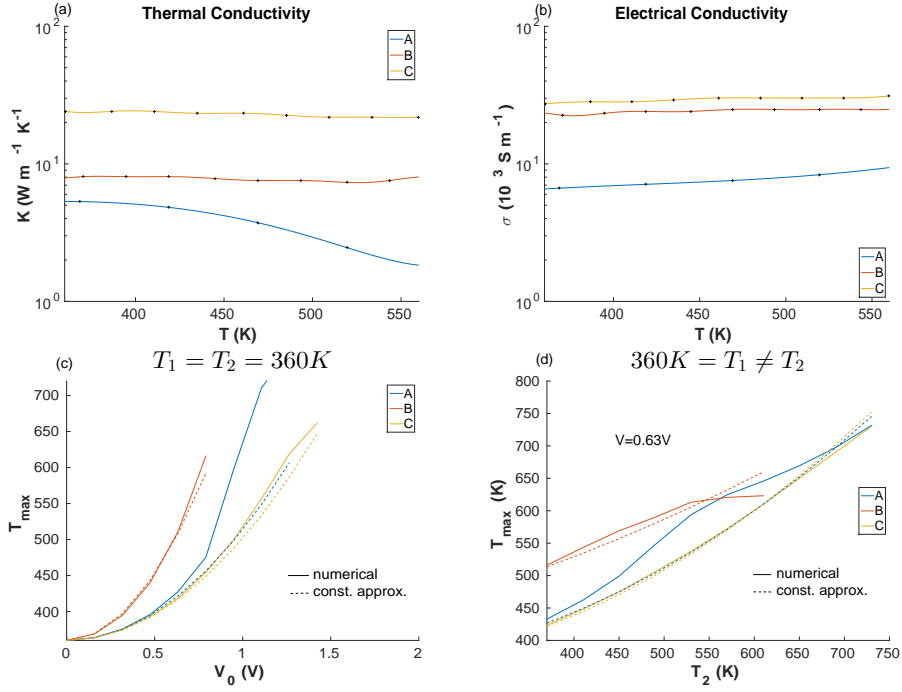
Figure 3.9: Carbon nanotube fibers (CNFs). (a) Thermal conductivity $\kappa(T)$ and (b) electrical conductivity $\sigma(T)$ taken from samples A-C in Fig. 3 of Ref. [12]. Lines in (a) and (b) are polynomial fits to the data points. (c) T_{max} as a function of V_0, for $T_1 = T_2 = 360$ K. (d) T_{max} as a function of T_2, for $V_0 = 0.63$ V and $T_1 = 360$ K. In (c) and (d), we assume $L = 1$ μm, solid lines are for numerical calculation using $\kappa(T)$ and $\sigma(T)$ in (a) and (b), and dashed lines are for the constant approximation conductivities, $\sigma(T) = \sigma(T = 360$ K), and $\kappa(T) = \kappa(T = 360$ K).
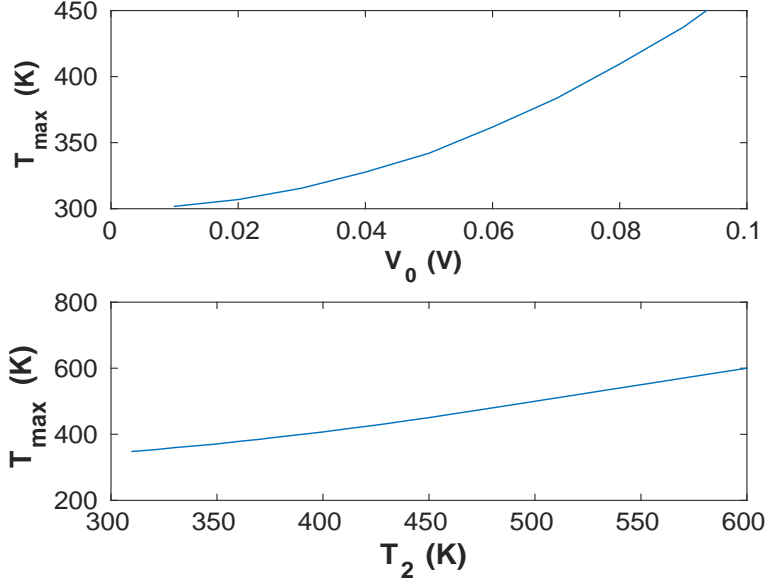
Figure 3.10: Copper with WF law. (a) T_{max} as a function of V_0, for $T_1 = T_2 = 300$ K. (b) T_{max} as a function of T_2, for $V_0 = 0.63$ V and $T_1 = 300$ K. $L = 1$ μm is assumed in the calculations.

3.3 Comparison of Theory and Experimental Results

While no experimental work was done as part of this research an experiment has used this theory to predict maximum temperatures of carbon nanotube (CNT) fibers during field emission [51]. The experiment was performed at the Air Force Research Laboratory. In this experiment a straight and a looped CNT fiber were attached to a cathode and biased to achieve an emission current of 3 mA in an attempt to explain differences in their operation. Thermal images were captured to obtain the maximum temperature of each as well as the position where this emission was achieved (Fig 3.11). Furthermore, the thermal and electrical conductivities were measured and a prediction was made for the maximum temperature and its position along the wire while assuming constant κ and σ, as well as while assuming constant σ and a linear dependence of $\kappa(T)$. Finally, numerical results were obtained assuming a linear dependence for $\sigma(T)$ and a polynomial fit for $\kappa(T)$. The results are presented on Table 1, which is taken directly from [51].
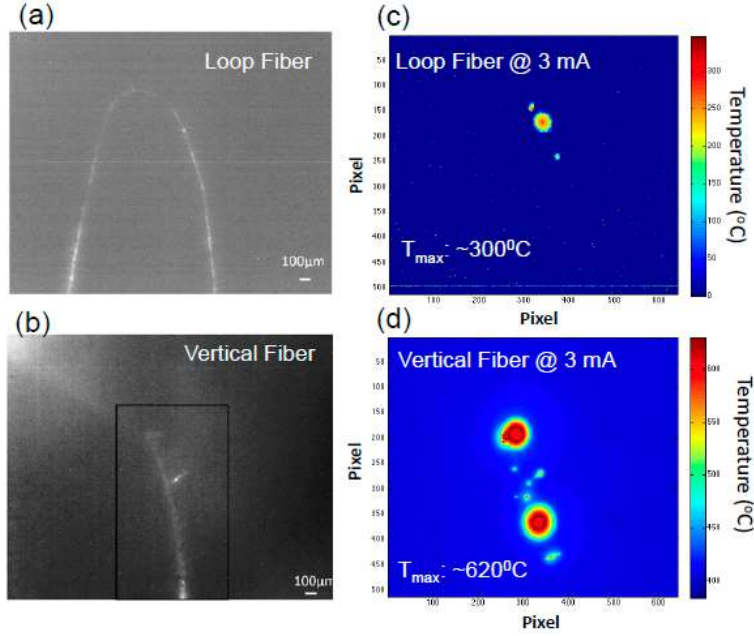
Figure 3.11: Optical image of the (a) looped CNT fiber and (b) single vertical CNT fiber. Temperature distribution of the (c) looped CNT fiber and (d) vertical CNT fiber, obtained from an IR camera. From [51]

Carbon Nanotube (CNT) Fiber Emitter		Measured	Constant σ and κ	Constant σ and Linear $\kappa(T)$	Linear $\sigma(T)$ and Polynomial Fit to $\kappa(T)$
Vertical	T_{max} [°C]	~600	580	595	600
	S_{max} [mm]	~3.0	4	3.5	3.1
Looped	T_{max} [°C]	~300	254	286	300
	S_{max} [mm]	~4	4	4	4

Table 3.1: Comparison of the measured maximum temperature and its location for both the vertical and looped fiber emitters, with this theory under various assumptions. From Ref. [51]

Assuming constant σ and κ gives bulk-part estimates for both T_{max} and z_{max} (the position where the maximum temperature occurred) but using a linear fit for $\kappa(T)$ reduces the error of predicted temperature by up to 10% while reducing the error in the position where the maximum temperature occurred by up to 16%. This comparison demonstrates the applicability of the 1D analysis presented in this chapter, and the relative merits in various models of $\kappa(T)$ and $\sigma(T)$.

3.4 Summary

In this chapter, we evaluate the effects of temperature dependence of the electrical and thermal conductivities on the Joule heating of a one-dimensional conductor, by solving the coupled non-linear steady state electrical and thermal conduction equations. We found that there are conditions under which no steady state solution exists. In the special case of constant electrical conductivity and linear temperature dependence of the thermal conductivity, we have obtained explicit expressions for the bounds of existence of solutions. The shifting of these bounds due to the introduction of linear temperature dependence of electrical conductivity is also examined. The temperature distribution, the maximum temperature and its location within the conductor are examined for various temperatures imposed at the ends of the 1D conductor. Sample calculations for carbon nanotube fibers and copper are demonstrated and the theory has been favorably compared with experiments. We note that the absence of a steady state solution may indicate the occurrence of thermal runaway. This may be a topic for future research. Additional topics include the stability of the steady state and the effects of thermal insulation (zero heat flux boundary condition) imposed on one end of the sample.

Chapter 4. Absolute instability and transient growth near the band edges of a traveling wave tube

This chapter is dedicated to exploring the absolute instability near the upper and lower band edges of the amplification band. While section 1.3 gave an overview of absolute instability, section 4.1 further defines the scope of our investigations. Section 4.2 presents the model, and the stability criterion for the onset of absolute instability at the lower and upper band edges, A and B (Fig. 4.1). There we show that the upper band edge is more susceptible to absolute instability than the lower band edge. Section 4.3 presents the Green's function constructed from the dispersion relation. Its asymptotic form shows the transition from transient exponentiation at fractional power of time to simple exponential growth (to decay) when the band edge is (is not) subject to an absolute instability. Section 4.4 presents concluding remarks. The details of the derivations are given in Appendix Appendix F.

4.1   Introduction

The circuit mode of a coupled cavity TWT is shown in Fig. 4.1, whose lower or the upper band edge are respectively labeled as Points A and B. The beam mode, $\omega = kv$, intersects with the circuit mode in a forward wave amplifier at the operating point Q, which lies between A and B. Potential excitation of absolute instability at band edges A and B for such a forward wave amplifier have been studied by Kuznetsov et al. [69], and by Hung et al. [70] using the Briggs-Bers criterion [74, 75]. Both papers reported that, for an operating point Q, an absolute instability can occur at the upper band edge, but not the lower band edge. Since the lower band edge was (erroneously, as we discovered in this thesis) perceived as to be free of absolute instability, we attempted to assess the possible transient growth at the lower band edge. In this re-examination of the lower band edge, we discovered that the lower band edge does suffer from absolute instability when the beam current is sufficiently high, contrary to the earlier findings. This chapter reports this revised study. In addition, we present the newly derived stability criterion for the onset of absolute instability at both band edges, from which we conclude that the upper band edge is more susceptible to absolute instability than the lower band edge. We also show transient temporal growths with exponentiation rate proportional to $t^{1/3}$, whether or not the band edge is subject to an absolute instability.

Transient growth at a fractional power of time is an interesting characteristic at the band edges, a possibility suggested by Hung et al. [70]. A zero group velocity at the band edge means that, electromagnetically, a unit in a periodic structure is isolated from its neighbor. Information is carried only by the beam. This is precisely the condition in the formulation of the cumulative beam breakup instability, originally studied by Panofsky and Bander for RF linacs [92], which was extended to high current induction accelerators by Hall,

Neil and Cooper [93], and to linear colliders by Chao, Richter, and Yao [94]. All of these authors found fractional power of growth in time, and their main results may all be recovered in a unified analysis by assuming a zero group velocity in the structure mode in a mode-coupling analysis [95]. Note that instability whose amplitude exponentiates at a fractional power of time (at a fixed position) is not covered by the Briggs-Bers criterion [74, 75], which only governs existence of instability that exponentiates as a linear function of time. Thus our study provides a first demonstration of transition from exponential growth at fractional power of time to simple exponential growth when the band edge suffers from absolute instability, and from exponential growth at fractional power of time to stabilization when the band edge is free from absolute instability. In fact, it is this interesting transition, not covered by the Briggs-Bers criterion, that prompted our re-examination of the band edge oscillations in the first place [71].
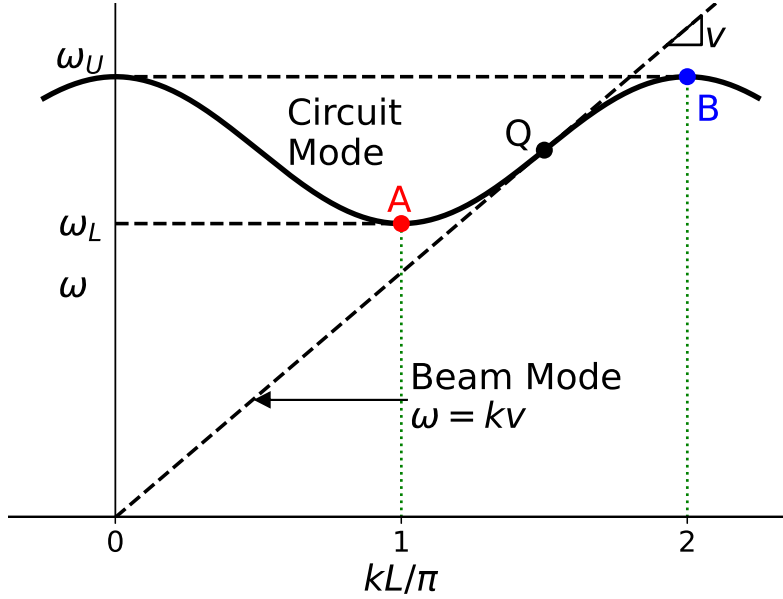
Figure 4.1: The dispersion diagram of a coupled cavity TWT, showing the lower band edge (A), the upper band edge (B), and the operating point (Q) at which the beam mode intersects with the circuit mode. kL is the phase shift per period, L is the period of the slow wave structure, and v is the DC velocity of the electron beam.

We should stress that the effects of end reflections are ignored in this chapter. That is, we assumed that the system is infinitely long, as in the Briggs-Bers criterion. This is a serious limitation for TWT stability analysis because the circuits are poorly matched at a band edge.

4.2 Existence of Absolute Instability

For interactions sufficiently close to the band edges, either at A or at B (Fig 4.1), the circuit mode dispersion relation can be well approximated as a hyperbola in the $\omega - k$ plane in the vicinity of A or B (Fig. 4.1). For a wave-like perturbation of the form $e^{i\omega t - ikz}$, the hot tube dispersion relation, near A or B, may then be represented as [67, 68, 70]

$$D(\omega, k) \equiv (\omega - kv)^2 \left[(\omega - \omega_m)^2 + 2\Delta(\omega - \omega_m) - r^2(k - k_m)^2 \right] - \omega_m^4 \varepsilon = 0 \quad (4.1)$$

where $(\omega, k) = (\omega_m, k_m)$ designates the band edge A or B, r and Δ are fitting parameters for the circuit mode dispersion relation at A or B, and ε is the dimensionless coupling constant between the beam mode ($\omega = kv$) and the circuit mode which is represented by the square bracket of Eq. (4.1). The coupling constant ε is proportional to the DC beam current in the classical theory of TWT [67, 68, 70]. Note that in [70] ω_m is defined as the focus of the hyperbola (see Fig. 4.2) that represents the circuit mode; this focus is $\omega_m - \Delta$ in the present chapter. For the lower (upper) band edge A (B), both Δ and ε are positive (negative) [70]. It remains finite at the band edges in a careful analysis. Away from the band edges, its magnitude is approximately equal to $2C^3$, where C is Pierce's gain parameter in a TWT [66–68]. We next applied the Briggs-Bers criterion [74, 75] to the dispersion relation, Eq. (4.1). With $\omega = \omega_m(1 + y)$, $k = k_m(1 + x)$, Eq. (4.1) is non-dimensionalized to read,

$$D(x, y) \equiv (y - ux + 1 - u)^2(y^2 + 2\delta y - \rho^2 x^2) - \varepsilon = 0 \quad (4.2)$$

where (ω, k) is now represented by (y, x) in normalized form, $u = k_m v / \omega_m$, $\delta = \Delta / \omega_m$, and $\rho = k_m / \omega_m$ The beam mode and the circuit modes are shown in Fig. 4.2a for the lower band edge, and in Fig. 4.2b for the upper band edge. In these plots, and in the numerical examples below, we used the parameters in Hung et al. [70]. For the lower band edge, $\Delta/2\pi = 7.365$ GHz, $r = 8.6973 \cdot 10^9$ m/s, $k_m = 1.78$mm^{-1}, $\omega_m/2\pi = 24.24$ GHz. For the upper band edge, $\Delta/2\pi = -7.365$ GHz, $r = 8.6973 \cdot 10^9$ m/s, $k_m = 3.560$ mm^{-1}, $\omega_m/2\pi = 36.96$ GHz. These parameters model a realistic coupled-cavity TWT.
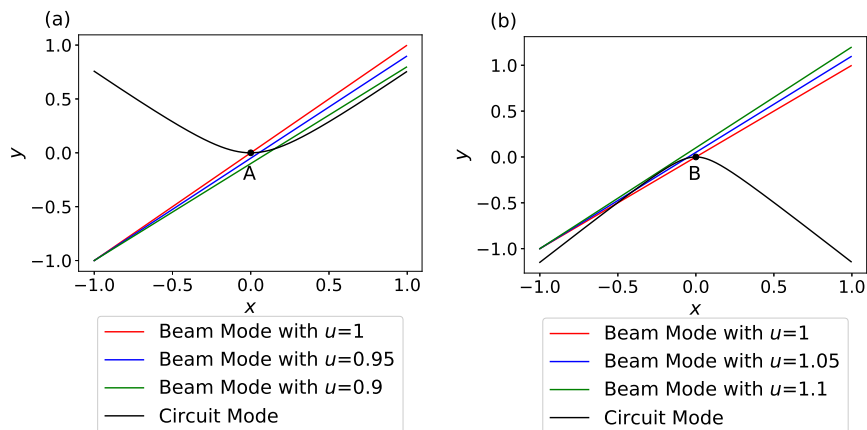
Figure 4.2: Normalized dispersion relation for circuit mode and beam mode at different beam velocities for (a) left, lower band edge A, and (b) right, upper band edge B. The hyperbola representing the circuit mode is concave (convex) at the lower (upper) band edge

To apply the Briggs-Bers criterion on the existence of absolute instability, we first solve the system [74, 75]

$$D(x, y) = 0 \tag{4.3a}$$

$$\frac{\partial D}{\partial x} = 0 \tag{4.3b}$$

which will yield eight pairs of solutions (x_s, y_s). x_s is guaranteed to be a double root (or higher order root) of $D(x, y) = 0$ for $y = y_s$. Such a double root (or higher order root) implies absolute instability if:

- y_s has a negative imaginary component, and

- Taking the imaginary component of y from y_s to minus infinity, at least a pair of x such as $D(x, y) = 0$ splits from the double (or multiple) root x_s to opposite imaginary infinities.

Specifically, the absolutely unstable solutions will have a normalized growth rate of $Im(y_s)$. We apply numerical methods to check the Briggs-Bers criterion and then analytically find the threshold value of ε for the onset of absolute instability. The details of the derivation are given in Appendix Appendix F. We summarize the results below. We confirmed the well-known result that absolute instability always occurs when the beam and circuit modes intersect at a negative group velocity point ($kL/\pi \notin [1, 2]$ for the example in Fig. 4.1) for all nonzero beam current, and these absolute instabilities have been known as backward wave oscillations [66, 72, 96]. For interactions with positive group velocity ($kL/\pi \in (1, 2)$) absolute instability is found for both the upper and the

42

lower band edges. The normalized threshold current is analytically calculated as (see Appendix Appendix F)

$$\varepsilon_{lower} = \left(\frac{u((1-u)^2 - 2\Delta(1-u))}{2\rho} \right)^2 \qquad (4.4)$$

for the lower band edge, and as

$$\varepsilon_{upper} = -27/256\kappa^4 u^2 \rho^2 \qquad (4.5a)$$

$$\kappa = \frac{-8u(\Delta + u - 1) + 2\sqrt{16\Delta^2 u^2 - 2\rho^2((u-1)^2 + 2\Delta(u-1)}}{8u^2 + \rho^2} \qquad (4.5b)$$

for the upper band edge. Figure 4.3 shows that the threshold ε for the upper band edge is orders of magnitude smaller than it is for the lower band edge, for similar deviation of the operating point, Q, from points A and B in Fig. 4.1. This implies that the upper band edge is significantly more prone to absolute instability than the lower band edge. While the dispersion relation (Eq. (4.1)) for the upper and lower band edges are normalized differently, for the same current, the value of ε typically differs only by a factor of order unity between the lower and upper band edge.
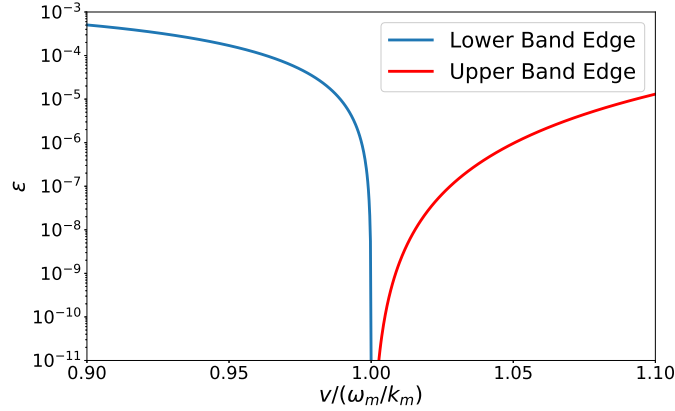
Figure 4.3: Threshold values of ε for lower band edge ($v < \omega_m/k_m$) and upper band edge ($v > \omega_m/k_m$). The phase velocity of the circuit mode at either band edge is ω_m/k_m.

4.3 Temporal Evolution of Green's Function

When the TWT is not subjected to an absolute instability, an initial perturbation may still undergo transient growth (at a fixed position z) before the perturbation is convected away. There will also be transient growth in the perturbations before simple exponential growth when an absolute instability is

present. The Green's function, which is the response to an impulse excitation at t = 0, and z = 0, would show both properties [74, 75]. From the dispersion relation, Eq. (4.1), the Green's function may be constructed [74, 75, 92, 95]

$$G(z,t) = \int d\omega \int dk \frac{e^{i(\omega t - kz)}}{D(\omega, k)} \propto \int d\omega \, e^{i(\omega t - k(\omega)z)} \tag{4.6}$$

where $k(\omega)$ is the solution to $D(\omega, k) = 0$. In the evaluation of the Green's function, Eq. (4.6), it is found that the dominant term in the exponents of the asymptotic expansion of the last integral of Eq. (4.6) gives an adequate approximation for the temporal evolution, including exponentiation at fractional power of t [92, 95, 97]. Thus, we use the saddle point method, and approximate Eq. (4.6) as,

$$G(z,t) \propto e^{i(\omega_s t - k_s z)} \tag{4.7}$$

where (ω_s, k_s) is the meaningful root that satisfies

$$D(\omega_s, k_s) = 0 \tag{4.8a}$$

$$\left(\frac{\partial D}{\partial \omega} + \frac{t}{z} \frac{\partial D}{\partial k} \right) \Bigg|_{\omega_s, k_s} = 0 \tag{4.8b}$$

We express the magnitude of Eq. (4.7) in exponential form, $\exp[kzf(T)]$, where $T = (\omega_m t)/(k_m z)$. Figure 4.4a shows the time dependence of $f(T)$ for the lower band edge when it is stable, marginally stable, and unstable against absolute instability. In all three cases, $f(T) \propto T^{1/3}$, transiently for small T (Fig. 4.4a). The same is true in the upper band edge, as shown in Fig. 4.4b. When absolute instability exists, both Figs. 4.4a and 4.4b show that f(t) transitions from $f(T) \propto T^{1/3}$ to $f(T) \propto T$ for large T. Note that these explicit calculations of the Green's function validated the stability criterion, Eqs. (4.4) and (4.5). Figures 4.4a and 4.4b show the transition from the transient exponentiation at fractional power of t (at fixed z) to simple exponential growth when there is an absolute instability in the sense of Briggs and Bers. When the TWT is not subjected to an absolute instability, an initial perturbation may still undergo transient growth (at a fixed position z) before the perturbation is convected away, as also shown in Figs. 4.4a and 4.4b.

44
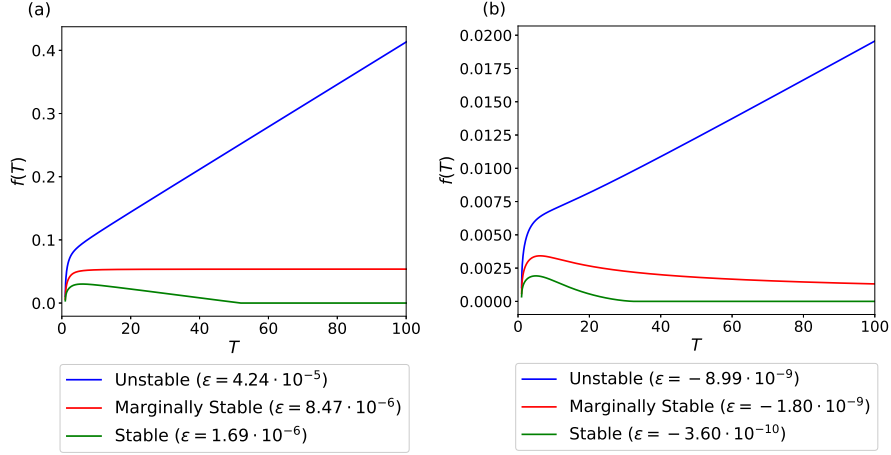
Figure 4.4: f(T) for (a) left, the lower band edge with $v = 0.99\omega_m/k_m$ (b) right, upper band edge with $v = 1.01\omega_m/k_m$. Note that ε is roughly $2C^3$, where C is the gain parameter. A comparison of ε at marginal stability between the two shows that the upper band edge is more susceptible to absolute instability than the lower band edge.

Alternatively, we can express Eq. (4.7) in exponential form, $\exp[\omega_m t\, g(Z)]$, where $Z = (k_m z)/(\omega_m t)$ and $g(Z)$ is shown in Fig. 4.5. As seen from Figs. 4.5a and 4.5b, $g(Z)$ will have very similar shapes for unstable and stable cases, and for both lower and upper band edge. These two figures essentially give the spatial distribution of the logarithm of the Green's function as given by Eq. (4.7), from the beam head ($Z = 1$, or $z/t = \omega_m/k_m \simeq v$) to the beam tail (Z = 0) in a continuous beam. The key difference between stability and instability lies close to $Z = 0$, i.e., as $t \to \infty$. Thus, the cases where $g(0) > 0$ correspond to absolute instability whereas the cases where $g(Z) \leq 0$ for some $Z < Z_0$ correspond to absence of absolute instability. Note that the lower band edge has larger exponents in the Green's function; it is caused by the much higher values of ε that are required to excite an absolute instability.

45
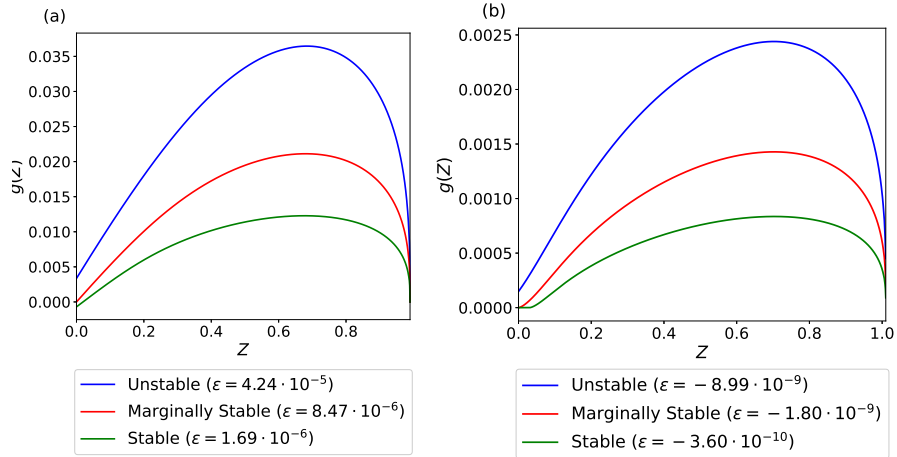
Figure 4.5: $g(Z)$ for three cases according to Briggs-Bers criterion: unstable, marginally stable, and stable. (a) left, the lower band edge with $v = 0.99\omega_m/k_m$ and (b) right, the upper band edge with $v = 1.01\omega_m/k_m$.

4.4 Concluding Remarks

In this chapter, we show that the Green's function, at a fixed position z, exponentiates transiently at a rate proportional to $t^{1/3}$, when the beam mode intersects the circuit mode at a point very close to the band edge, regardless of whether there is an absolute instability or not. This statement applies to both upper and lower band edge, and the transient growth will turn into simple exponential growth if there is an absolute instability, but will decay in time if absolute instability is absent. This may be understood as follows. Very close to the band edge, the dispersion relation for the circuit mode behaves like a straight line, $\omega - \omega_m = 0$, i.e., it has zero group velocity, and the beam-circuit interaction may then be described by, when written in the form of Ref. [95],

$$D(\omega, k) \equiv (\omega - kv)^2(\omega^2 - \omega_m^2) - \omega_m^4 \varepsilon = 0 \qquad (4.9)$$

whose Green's function indeed exponentiates as $t^{1/3}$, first discovered by Panofsky and Bander [92]. If one still assumes operation very close to the band edge, so that the assumption of zero group velocity still holds (i.e., $\omega - \omega_m = 0$), but includes the "space charge effects" in the beam mode, Eq. (4.9) is modified to read [67, 68],

$$D(\omega, k) \equiv \left((\omega - kv)^2 - \omega_q^2\right)(\omega^2 - \omega_m^2) - \omega_m^4 \varepsilon = 0 \qquad (4.10)$$

In Eq. (4.10), ω_q^2 is the square of plasma frequency that includes the plasma reduction factor, and it represents the space charge effect, QC, in Pierce theory of traveling wave tube [66–68]. The Green's function to the dispersion relation of the form Eq. (4.10) was studied in great detail in [95], which always show

46

transient growth at a fractional power of time. This transient growth could be different from $t^{1/3}$, depending on the magnitude of ω_q^2, ε , and z [95]. Thus, including the space charge effects of a TWT, very close to the band edge, the Green's function still exponentiates transiently at some fractional power of time, before the asymptotic behavior (at fixed z) predicted by the Briggs-Bers criterion appears. In summary, when the beam mode intersects with the forward circuit mode of a slow wave structure, an absolute instability exists at both the lower and upper band edges, if the beam current is sufficiently high. The upper band edge is more susceptible to absolute instability than the lower band edge. The threshold condition for the onset of absolute instability at both band edges is given. Close to a band edge, there is always transient growth in the Green's function, at a fractional power of time, whether or not there is an absolute instability.

Finally, we emphasize that absolute instability is not easy to identify experimentally on a traveling wave tube in general. One reason is that TWT may be subjected to a host of other instabilities, such as the backward wave oscillations and regenerative oscillations. In addition, at the band edges, the group velocity is zero, where the waveguide circuits are difficult to match, and the instability fluctuations are not readily coupled out. But absolute instability has indeed been detected in experiments on the gyrotron traveling wave amplifiers [98], a topic which has been studied in great details in the gyrotron community. See the extensive review by K. R. Chu, Rev. Mod. Phys. 76, 489 (2004). There appears to be no published experiment documenting absolute instability in a conventional TWT.

Chapter 5. Conclusions

This thesis considers three topics of contemporary interest to the study of electron device, individually treated in Chapters 2, 3, and 4. In Chapter 2, we presented a novel theory of electrical contact resistance under AC condition. We considered an AC current flowing through two Cartesian current channels joined together. Each current channel may be made of different materials and may have different dimensions. Because of the resistive skin effects, especially at high frequencies, the currents flow mainly within the respective skin depths from the boundaries of the respective current channels, including the contact region. The contact resistance, therefore, is higher than the DC case in general. We found an exception to this rule, namely, at some frequencies, the contact resistance may become negative, meaning that the total resistance is less than the bulk resistance from the individual current channels. This unusual result is interpreted as reduced current crowding near the joined region. We have treated various geometries, including slightly uneven joints. The respective skin depths, the channel dimensions, then become important parameters. Scaling laws of the contact resistance have been derived in different frequency regimes. We should stress that the theory of AC contact resistance is challenging and complex, which leaves many research topics for future works. For example, our theory is primarily applied to current channels that satisfies $\omega\varepsilon \ll \sigma$, where ω is the frequency, ε is the permittivity, and σ is the electrical conductivity in the respective channel. We have not explored materials outside this range, which include poor conductors or semiconductors. The series representation for the electromagnetic fields converge much slower for the latter materials. We have not found a consistent definition for the other lumped parameters, the inductance or capacitance. Even under the assumption $\omega\varepsilon \ll \sigma$, we have not entirely solved for the AC field solution at the triple point, which is the intersection of the two current channels and their surrounding vacuum region. These are worthy areas of study whose solution is also of immense computational interest.

Chapter 3 presents a nonlinear, steady state, theory of thermal and electrical conduction on a 1-dimensional conductor with a specified temperature dependence in the thermal and electrical conductivities. Several representative models of temperature dependence were explored, where in some cases, the spatial temperature distribution may be calculated analytically, and the regime for the existence of solution predicted. Such solution was used successfully in interpreting the experimentally observed temperature distribution on a carbon nano-fiber field emitter. Interesting topics for future investigation include the sinusoidal steady state solution, which is relevant when the field emitters are modulated to create a bunched electron beam for the generation of coherent radiation. A time-dependent solution will also be a valuable contribution to the study of electrothermal instabilities and of thermal runaway. The steady state solutions developed in this chapter need to be extended to 2-dimensions, which would be of immense interest to the study of electromigration in semiconductor junctions. The heating of a conical conductor with a voltage applied at different

heights would produce interesting and useful results.

Finally, in Chapter 4 the absolute instability at the band-edges of a traveling wave tube (TWT) is re-examined. We overturned the previously established results which claim that absolute instability at the lower band edge does not exist when the TWT operates in the forward wave mode of the waveguide circuit. We found that absolute instability at the lower band edge does exist, but occurs at a higher threshold in the electron beam current than at the upper band edge. The temporal-spatial evolution of the Green's function was also calculated for the first time on a TWT model, showing exponential growth at a fractional power of time initially, followed by simple exponential growth in time or decay in time, depending on whether the current threshold for absolute instability is exceeded. More accurate modelling of TWT dispersion relation is desirable, including the modifications of the beam mode and circuit modes by the AC space charge effects. However, experimental identification of absolute instability studied in this thesis would be difficult for a TWT, because of poor matching of the circuit at band edges. In addition, the absolute instability might be masked by regenerative oscillations, caused by reflections from the ends of the waveguide circuit, or by the backward wave oscillations that have been extensively treated for TWT.

Appendix A. Full Solution of AC Contact Resistance
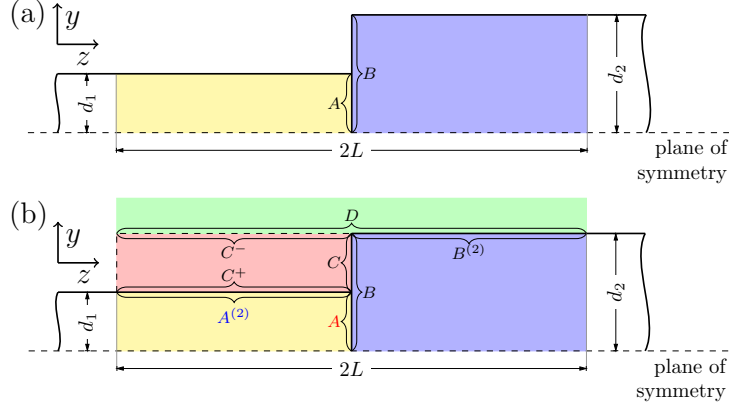
Figure 5.1: The colored regions, which are considered, as well as the boundary terms for the DC case (a) and the AC case (b).

First let us consider the DC case (Fig. 5.1a). To satisfy the boundary conditions (2.2a-2.2c) we include fields in each conductor with the following form:

$$E_{z,A} = \sum_{n=1}^{\infty} A_n \cos\left(\frac{n\pi y}{d_1}\right) e^{\frac{n\pi z}{d_1}} \tag{5.1a}$$

$$E_{y,A} = \sum_{n=1}^{\infty} -A_n \sin\left(\frac{n\pi y}{d_1}\right) e^{\frac{n\pi z}{d_1}} \tag{5.1b}$$

in the left conductor and

$$E_{z,B} = \sum_{n=1}^{\infty} B_n \cos\left(\frac{n\pi y}{d_2}\right) e^{-\frac{n\pi z}{d_2}} \tag{5.2a}$$

$$E_{y,B} = \sum_{n=1}^{\infty} -B_n \sin\left(\frac{n\pi y}{d_2}\right) e^{-\frac{n\pi z}{d_2}} \tag{5.2b}$$

in the right conductor. These fields are chosen to enforce symmetry around the y=0 plane, the plane of symmetry, as well as to ensure that (2.2d) and (2.2e) are satisfied. Note that the bulk fields (2.5) need to be added to (5.1) and (5.2) to obtain the total fields in each conductor. Field "A" will be used to satisfy (2.2b) and Eq. (5.1) is therefore a Fourier representation over $(z = 0, y \in [0, d_1])$ while field "B" will be used to satisfy (2.2a) and (2.2c) and Eq. (5.2) is therefore a Fourier representation over $(z = 0, y \in [0, d_2])$. In Fig. 5.1a, these regions can be seen. Next, we truncate the Fourier series for each field to N terms, since

convergence was proven in [64]. This allows us to use (2.2a-2.2c) to obtain a $2N \times 2N$ matrix that can be inverted to yield A_n and B_n, and therefore the fields everywhere.

Moving on to the AC case the boundary conditions now have the following form (Fig. 5.1b)

$$E_{y,1} = E_{y,2}, \qquad\qquad\qquad\qquad\qquad z = 0, |y| < d_1 \quad (5.3a)$$

$$(\sigma_2 - i\omega\varepsilon_2)E_{z,2} = \begin{cases} (\sigma_1 - i\omega\varepsilon_1)E_{z,1}, & |y| < d_1 \\ -i\omega\varepsilon_0 E_{z,3}, & d_1 < |y| < d_2 \end{cases}, \quad z = 0 \qquad (5.3b)$$

$$E_{z,1} = E_{z,3}, \qquad\qquad\qquad\qquad\qquad |y| = d_1, z < 0 \quad (5.3c)$$

$$(\sigma_1 - i\omega\varepsilon_1)E_{y,1} = (-i\omega\varepsilon_3)E_{y,3}, \qquad\qquad |y| = d_1, z < 0 \quad (5.3d)$$

$$E_{y,2} = E_{y,3}, \qquad\qquad\qquad\qquad\qquad z = 0, d_1 < |y| < d_2 \qquad\qquad\qquad\qquad\qquad\qquad\qquad\qquad (5.3e)$$

$$E_{y,3} = E_{y,4}, \qquad\qquad\qquad\qquad\qquad |y| = d_2, z < 0 \quad (5.3f)$$

$$(\sigma_2 - i\omega\varepsilon_2)E_{y,2} = -i\omega\varepsilon_0 E_{y,4}, \qquad\qquad |y| = d_2, z > 0 \quad (5.3g)$$

$$E_{z,4} = \begin{cases} E_{z,3}, & z < 0 \\ E_{z,2}, & z > 0 \end{cases}, \qquad\qquad\qquad |y| = d_2 \qquad (5.3h)$$

where E_1 corresponds to fields withing the left current channel (yellow region in Fig. 5.1b), E_2 corresponds to fields withing the right current channel (blue region in Fig. 5.1b), E_3 corresponds to fields within ($z \in [-L, 0]$, $y \in [d_1, d_2]$) (red region in Fig. 5.1b) and E_4 to fields within ($z \in [-L, L]$, $y \in [d_2, \infty]$) (green region in Fig. 5.1b). To satisfy all of the above we need to include a field that is a Fourier transform for each boundary condition. All the regions that have a Fourier transform over them can be seen in Fig. 5.1b. For example, the resulting total $E_{z,1}$ in the conductor to the left is:

$$E_{1,z} = \frac{I_0 \kappa_1}{2W\sigma_1} \frac{\cos(\kappa_1 y)}{\sin(\kappa_1 d_1)} \qquad\qquad\qquad\qquad \text{(bulk solution)}$$

$$+ \sum_{n=1}^{\infty} A_n \cos\left(\frac{n\pi y}{d_1}\right) \exp\left(z\sqrt{\left(\frac{n\pi}{d_1}\right)^2 - \kappa_1^2}\right) \qquad \text{(meant to satisfy (5.3a))}$$

$$+ \sum_{n=1}^{\infty} A_n^{(2)} \sin\left(\frac{(2n-1)\pi z}{2L}\right) \cosh\left(y\sqrt{\left(\frac{(2n-1)\pi}{2L}\right)^2 - \kappa_1^2}\right) \quad \text{(meant to satisfy (5.3d))}$$

where κ_1 is defined in Eq. (2.6). Numerically, the last infinite sum is very small for all cases studied in this chapter. Truncating all series to N and using the eight boundary conditions (5.3a-5.3h) in the fields of all other regions we can obtain a $8N \times 8N$ matrix which can again be solved numerically. Doing so however requires 16 times more memory and ≈ 64 times more time than the DC case with the same N. For $\sigma \gg \varepsilon\omega$ (5.3a-5.3h) turn into (2.2a-2.2e)

and we only need fields "A" and "B" in Fig. 5.1a again and then use the boundary matching techniques given in [64]. Note that the "A" and "B" in Fig. 5.1a solutions satisfy the Laplace (Helmholtz) equation for the DC (AC) case. Comparing the full solution utilizing all 8 Fourier fields to the simplified solution for $\sigma \geq 3.69 \cdot 10^5$ S/m and $\omega/2\pi \leq 10$ THz we obtain contact resistances within 0.000042% of each other. For semiconductors the full solution would need to be used, but L needs to be much larger consequently and a larger N needs to be used for proper accuracy.

Appendix B. Bulk Solutions for the AC Case

Solving Maxwell's equations under the AC conditions in a conductor (Fig 2.1) yields fields that are proportional to

$$F(z,y) = e^{ik_z z} e^{ik_y y} \tag{5.4a}$$

$$k_z^2 + k_y^2 = \kappa^2 \equiv \mu\varepsilon\omega^2 + i\omega\mu\sigma \tag{5.4b}$$

For the bulk currents in each conductor we have $k_z = 0$ and $E_y = 0$. Furthermore fields need to be symmetric around the $y = 0$ axis. This means that the only field in each conductor are:

$$E_{z,1,b} = E_1 \cos(\kappa_1 y), \qquad\qquad |y| < d_1 \tag{5.5a}$$

$$E_{z,2,b} = E_2 \cos(\kappa_2 y), \qquad\qquad |y| < d_2 \tag{5.5b}$$

where E_1 and E_2 are complex constants. To find their respecting values we solve

$$W \int_{-d_1}^{d_1} \sigma E_{z,1,b} dy = I_0 \tag{5.6a}$$

$$W \int_{-d_2}^{d_2} \sigma E_{z,2,b} dy = I_0 \tag{5.6b}$$

to obtain

$$E_1 = \frac{I_0 \kappa_1}{2W\sigma_1} \frac{1}{\sin(\kappa_1 d_1)} \tag{5.7a}$$

$$E_2 = \frac{I_0 \kappa_2}{2W\sigma_2} \frac{1}{\sin(\kappa_2 d_2)} \tag{5.7b}$$

which can be used with (5.5) to yield equation (2.5) of the main text. To obtain the bulk resistance we first consider $\sigma \gg \omega\varepsilon$, so that (2.6) gives,

$$\kappa_1 \simeq \frac{1+i}{\delta_1} \tag{5.8a}$$

$$\kappa_2 \simeq \frac{1+i}{\delta_2} \tag{5.8b}$$

The average power dissipated in each conductor will be:

$$P = \sigma \int_V \left(\frac{|\boldsymbol{E}|^2}{2} \right) dV \tag{5.9}$$

Using this we now obtain the time averaged power per unit length for the left conductor

$$\frac{dP_1}{dl} = \frac{I_0^2}{4W\sigma_1\delta_1^2} \int_{-d_1}^{d_1} \frac{\cos\left(\frac{1+i}{\delta_1}y\right)\cos\left(\frac{1-i}{\delta_1}y\right)}{\sin\left(\frac{1+i}{\delta_1}d_1\right)\sin\left(\frac{1-i}{\delta_1}d_1\right)} dy \tag{5.10}$$

Using

$$\sin\left((1+i)x\right)\sin\left((1-i)x\right) = \frac{1}{2}\left(\cosh(2x) - \cos(2x)\right)$$

$$\cos\left((1+i)x\right)\cos\left((1-i)x\right) = \frac{1}{2}\left(\cosh(2x) + \cos(2x)\right)$$

we obtain

$$\frac{dP_1}{dl} = \frac{I_0^2}{2W\sigma\delta_1} \frac{\sinh\left(\frac{2d_1}{\delta_1}\right) + \sin\left(\frac{2d_1}{\delta_1}\right)}{\cosh\left(\frac{2d_1}{\delta_1}\right) - \cos\left(\frac{2d_1}{\delta_1}\right)} \tag{5.11}$$

Equating this to $RI_0^2/2L$ because of (2.3) we obtain

$$R_{b1} = \frac{L}{2W\sigma_1\delta_1} \frac{\sinh\left(\frac{2d_1}{\delta_1}\right) + \sin\left(\frac{2d_1}{\delta_1}\right)}{\cosh\left(\frac{2d_1}{\delta_1}\right) - \cos\left(\frac{2d_1}{\delta_1}\right)} \tag{5.12}$$

Similarly, for the second conductor one can obtain

$$R_{b2} = \frac{L}{2W\sigma_2\delta_2} \frac{\sinh\left(\frac{2d_2}{\delta_2}\right) + \sin\left(\frac{2d_2}{\delta_2}\right)}{\cosh\left(\frac{2d_2}{\delta_2}\right) - \cos\left(\frac{2d_2}{\delta_2}\right)} \tag{5.13}$$

Equations (5.12) and (5.13) are equation (2.8) from in chapter 2.2.

Appendix C. $\overline{R_c} \propto \omega^{1/2}$ Derivation

As ω increases, the skin depths, δ_1 and δ_2 will decrease. This means that at sufficiently high frequencies the following will be true (Fig 2.1):

$$\delta_1 \ll d_1 \tag{5.14a}$$

$$\delta_2 \ll d_2 \tag{5.14b}$$

$$\delta_2 \ll d_2 - d_1 \tag{5.14c}$$

When the above are true the current will be confined to the edges of the conductors. Such a current flow can be seen in Fig. 2.6 of the main text. The horizontal currents in each conductor are the bulk currents, which do not contribute to the contact resistance. The only remaining currents to consider are: The vertical current between points M and K as well as current perturbations to attain transitions that satisfy all relevant boundary conditions. The latter perturbations however will be confined to areas that are in order of δ_1^2 or δ_2^2, whereas the vertical current will occupy an area in the order of $(d_2 - d_1)\delta_2$. From Eq. (5.14) $\delta_2^2 \ll (d_2 - d_1)\delta_2$. Furthermore

$$\frac{\delta_1^2}{(d_2 - d_1)\delta_2} \propto \omega^{-\frac{1}{2}} \tag{5.15}$$

For sufficiently high frequencies we can also therefore assume $\delta_1^2 \ll (d_2 - d_1)\delta_2$. Because of the above we can assume that the contact resistance will only arise from the vertical current between points M and K. The current distribution in this area is approximately

$$J = \frac{I_0}{W\delta_2} e^{-\frac{z}{\delta_2}} \tag{5.16}$$

which will dissipate a total power of

$$P = \int_{d_1}^{d_2} dy \int_0^W dx \int_0^\infty \frac{J^2}{\sigma} dz = \frac{(d_2 - d_1)I_0^2}{2W\delta_2\sigma_2} \tag{5.17}$$

Equating the above with $R_c I_0^2 / 2$ as per (2.3) and normalizing using (2.9) we obtain

$$\overline{R_c} = 2\pi \frac{d_2 - d_1}{\delta_2} \propto \omega^{\frac{1}{2}} \tag{5.18}$$

which is Eq. (2.10) in section 2.3.

Appendix D. AC Triple Point

The general cylindrical solution to Maxwell's equations for the electric fields in the setup shown in Fig. 2.10 is

$$E_r = \left(A \frac{J_m(\kappa r)}{\kappa r} + B \frac{Y_m(\kappa r)}{\kappa r} \right) \left(c_1 e^{im\phi} + c_2 e^{-im\phi} \right) \tag{5.19a}$$

$$E_\phi = \frac{i}{m} \left(A J'_m(\kappa r) + B Y'_m(\kappa r) \right) \left(c_1 e^{im\phi} - c_2 e^{-im\phi} \right) \tag{5.19b}$$

where $J_m(x)$ is the Bessel function of the first kind, $Y_m(x)$ is the Bessel function of the second kind and κ is defined in Eq. (2.6). Using the recurrence relations

$$\frac{2m}{x} Z_m(x) = Z_{m-1}(x) + Z_{m+1}(x)$$

$$2 Z'_m(x) = Z_{m-1}(x) - Z_{m+1}(x)$$

we can obtain more similar form between E_r and E_ϕ,

$$E_r = [A(J_{m-1}(\kappa r) + J_{m+1}(\kappa r)) + B(Y_{m-1}(\kappa r) + Y_{m+1}(\kappa r))] \left(c_1 e^{im\phi} + c_2 e^{-im\phi} \right) \tag{5.20a}$$

$$E_\phi = [A(J_{m-1}(\kappa r) - J_{m+1}(\kappa r)) + B(Y_{m-1}(\kappa r) - Y_{m+1}(\kappa r))] \left(c_1 e^{im\phi} - c_2 e^{-im\phi} \right) \tag{5.20b}$$

For $|\kappa r| \ll 1$, assuming m is a not a non-positive integer we can use the following asymptotic forms:

$$J_m(\kappa r) \simeq \frac{1}{\Gamma(m+1)} \left(\frac{\kappa r}{2} \right)^m \tag{5.21a}$$

$$Y_m(\kappa r) \simeq -\frac{\Gamma(m)}{\pi} \left(\frac{\kappa r}{2} \right)^{-m} + \frac{1}{\Gamma(m+1)} \left(\frac{\kappa r}{2} \right)^m \cot(m\pi) \tag{5.21b}$$

Furthermore, the electric field energy per unit length z around the triple point will be

$$u_E = \frac{\varepsilon}{2} \int_0^{2\pi} d\phi \int_0^{\delta r} r |\boldsymbol{E}|^2 dr \tag{5.22}$$

and needs to be finite for a small positive scalar δr. The above implies that that if $E \propto r^n$ then $n > -1$ to obtain a finite energy stored in the electric field. Since $Y_m \propto r^{-|m|}$ as $|\kappa r| \to 0$ then $Y_{m-1}(\kappa r) \pm Y_{m+1}(\kappa r)$ will always diverge as r^{-1} at best. This means that B=0 in Eq. (5.19). Using this with Eq. (5.21a) we obtain

$$E_r \simeq r^{m-1} \left(a e^{im\phi} + b e^{-im\phi} \right) \tag{5.23a}$$

$$E_\phi \simeq i r^{m-1} \left(a e^{im\phi} - b e^{-im\phi} \right) \tag{5.23b}$$

where all the constants were absorbed into a and b. When $\omega > 0$, κ is complex in conducting regions which makes $J_m(\kappa r)$ exponentially growing with r. This

is because fields at the triple point have to be seeded at some positive r in conductors. Implementing these fields is quite difficult as a result.

The boundary conditions that need to be satisfied are E_r and $(\sigma - i\omega\varepsilon)E_\phi$ to both be continuous. This produces a system of equations that can be written as

$$\boldsymbol{M}(m)\boldsymbol{v} = 0 \tag{5.24}$$

where v is a vector with 6 rows that includes all the values of a and b from Eq. (5.23). This need to have a non-trivial solution which implies

$$\det(\boldsymbol{M}(m)) = 0 \tag{5.25}$$

which can be solved numerically to yield the values of m that can satisfy all boundary conditions at once. Note that there are multiple solutions to the above, of which we chose the one with a real part from 0 to 1, to obtain diverging solutions that do not produce infinite electric energy around the triple point. For the DC case with $\sigma_1 = \infty$ and $\sigma_2 = \sigma_3 = 0$, m was solved exactly by Jordan et al. [86].

Appendix E. Derivation of $\overline{T_{max}}$ assuming Weidemann-Franz law holds

For the Weidemann-Frantz law holding, with $T_1 = T_2$ we have $\alpha = V_0^2/lT_1^2$, $\overline{\sigma}(0) = \overline{\sigma}(1) = 1$, $\overline{T}(0) = \overline{T}(1) = 0$. Due to symmetry, the maximum temperature occurs at $\overline{z} = 0.5$, $\overline{T}(0.5) = \overline{T_{max}}$, $\frac{d\overline{T}}{d\overline{z}}\big|_{0.5} = 0$. We have,

$$\overline{\kappa} = \overline{\sigma}(1 + \overline{T}) \tag{5.26}$$

$$\frac{d}{d\overline{z}}\left(\overline{\kappa}\frac{d\overline{T}}{d\overline{z}}\right) = -\alpha\frac{\overline{J_c}^2}{\overline{\sigma}} \tag{5.27}$$

$$\int_0^1 \frac{\overline{J_c}}{\overline{\sigma}}d\overline{z} = 1 \tag{5.28}$$

Integrating (5.27) from 0 to 1 with respect to $\overline{z}$ and using (5.28) for the right hand side we get:

$$\overline{\kappa}(1)\left.\frac{d\overline{T}}{d\overline{z}}\right|_1 - \overline{\kappa}(0)\left.\frac{d\overline{T}}{d\overline{z}}\right|_0 = -\alpha\overline{J_c} \tag{5.29}$$

Since $\overline{\kappa}(0) = \overline{\kappa}(1) = 1$ and because of symmetry $\frac{d\overline{T}}{d\overline{z}}\big|_1 = -\frac{d\overline{T}}{d\overline{z}}\big|_0$ we get

$$\left.\frac{d\overline{T}}{d\overline{z}}\right|_0 = \frac{\overline{J_c}}{2} \tag{5.30}$$

Now multiplying (5.27) by $(1 + \overline{T})\overline{\sigma}\frac{d\overline{T}}{d\overline{z}}$ and integrating, we get

$$\frac{1}{2}\left((1 + \overline{T})\overline{\sigma}\frac{d\overline{T}}{d\overline{z}}\right)^2 = -\alpha\overline{J_c}^2\left(\overline{T} + \frac{\overline{T}^2}{2}\right) + c \tag{5.31}$$

For $\overline{z} = 0.5$, since $\frac{d\overline{T}}{d\overline{z}} = 0$, so we get $c = \alpha\overline{J_c}^2(\overline{T_{max}} + \overline{T_{max}}^2/2)$. Plugging in $\overline{z} = 0$ in (5.31) and using (5.30) yields,

$$\overline{T_{max}} = \pm\sqrt{\frac{\alpha}{4} + 1} - 1 \tag{5.32}$$

For $\alpha = 0$ we should get $\overline{T_{max}} = 0$ so the (+) sign is chosen. Therefore, we obtain

$$\overline{T_{max}} = \sqrt{\frac{\alpha}{4} + 1} - 1 \tag{5.33}$$

which is Eq. (3.14) in the main text.

Appendix F. Thresholds of absolute instability at lower and upper band edge

In this Appendix, we outline the derivation of the analytic expressions, Eqs. (4.4) and (4.5), the threshold condition for the onset of absolute instability at the lower and upper band edge, respectively.

First, we argue the following points which apply to both the lower and upper band edges. Refer to Eq. (4.3).

A. At marginal stability $Im(y_s) = 0$.

B. There are four pairs of solutions (x_s, y_s) to (4.3) that are candidates for absolute instability.

C. If a pair of solutions (x_s, y_s) is complex then $(\overline{x_s}, \overline{y_s})$ is also a pair of solutions, where the bar denotes complex conjugate.

A holds true since as mentioned in section 4.2 the normalized growth rate is $Im(y_s)$ and the growth rate at marginal stability is zero.

For B we first obtain (x_s, y_s) by solving the system of equations (4.3), which becomes:

$$(y - ux + 1 - u)^2(y^2 + 2\delta y - \rho^2 x^2) - \epsilon = 0 \tag{5.34}$$

$$2(y - ux + 1 - u)(u(y^2 + 2\delta y - \rho^2 x^2) - \rho^2 x(y - ux + 1 - u)) = 0 \tag{5.35}$$

This system can then be manipulated into an eighth order polynomial of x (y) eliminating y (x) which has to equal 0. There are therefore eight pairs of solutions (x_s, y_s) to this system. However there are two branches to the circuit mode hyperbola, $y^2 + 2\delta y - \rho^2 x^2 = 0$. Each branch is responsible for four of the eight solutions. One of the branches is a mathematical artifact of our approximation and therefore only four pairs of solutions are candidates for absolute instability. Finally let us consider C. Here and in any other case the statement "(x_s, y_s) is complex" means "x_s has a nonzero imaginary part or y_s has a nonzero imaginary part". The left hand side of (5.34) and (5.35) can be rewritten as,

$$p(x, y) = \sum_i \sum_j a_{i,j} x^i y^j \tag{5.36}$$

with $a_{i,j}$ being real coefficients. It is easy to show that $p(\overline{x}, \overline{y}) = \overline{p(x, y)}$. Therefore if (x_s, y_s) is a solution to both (5.34) and (5.35) then $(\overline{x_s}, \overline{y_s})$ will be a solution also. We next treat the lower band edge and the upper band edge.

Lower Band Edge

In this section we will derive the condition for marginal stability for the lower band edge. First, we argue that out of the four pairs of solutions that are candidates for absolute instability two will always be real and two will always be complex. To do so we use Fig. 5.2. The upper branch of the hyperbola

is the branch that yields solutions that are candidates for absolute instability. The dashed lines represent the solution to $D(x, y) = 0$ and the crosses are the solutions to $\frac{\partial D}{\partial x} = 0$, or $\frac{dy}{dx} = 0$, which is the condition of zero group velocity. As ε increases the dashed lines will move away from both the circuit mode and the beam mode. The slope on each dashed line will always be 0 at exactly one point regardless of ε. Therefore, there are exactly two real pairs of solutions which, being real, cannot be candidates for absolute instability. The two remaining pairs of solutions have to be complex, and are candidates for absolute instability when ε is sufficiently large. We believe that [70] did not check the complex roots for absolute instability for the lower band edge because the existence of real roots is a sufficient condition for stability at the upper band edge (see the following Section). This results in the erroneous claim in [70] that the lower band edge does not suffer from absolute instability when the beam mode intersects the circuit mode at the forward wave side.
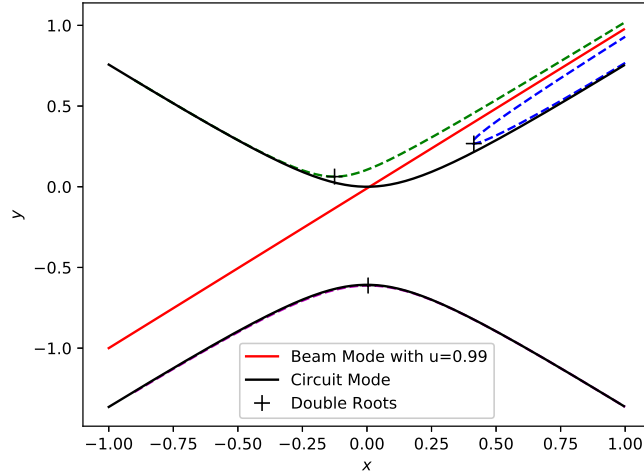
Figure 5.2: Graphical representation of solutions to (4.2) for the lower band edge for $\varepsilon = 10^{-3}$.

Numerically evaluating the Briggs-Bers criterion for the complex roots does yield absolute instability for sufficiently high values of ε. At marginal stability (x_s, y_s) must be complex and y_s must be real as argued in A. Therefore x_s must have an imaginary part. Furthermore $(\overline{x_s}, y_s)$ must also be a solution to (4.3) as argued in B. Since (4.3) guarantees that x_s and $\overline{x_s}$ are double roots of $D(x, y)|_{y_s} = 0$ then

$$D(x, y)|_{y_s} = a(x - x_s)^2(x - \overline{x_s})^2 = a(x^2 - 2\text{Re}(x_s)x + |x_s|^2)^2 \qquad (5.37)$$

for some real a. Using (4.2) to evaluate $D(x, y)|_{y_s}$ and setting each coefficient of the fourth order polynomials of x in Eq. (5.37) equal to each other we obtain a

system of five equations with five unknowns (ε, $\text{Re}(x_s)$, $|x_s|^2$, y_s and a). Solving this system yields Eq. (4.4) of the main text.

Upper Band Edge

In this section we will derive the condition for marginal stability for the upper band edge. First, we argue that out of the four pairs of solutions that are candidates for absolute instability two will always be complex and two will transition from real to complex as ε increases. Figure 5.3 shows the dispersion relation (4.2) for a high value of ε at which absolute instability exists. Figure 5.4 shows the dispersion relation (4.2) for a low value of ε at which absolute instability does not exist. In Fig. 5.3, the bottom branch of the hyperbola is the one that yields solutions that are candidates for absolute instability at the upper band edge. Figure 5.4 is zoomed in around the intersection point of the beam mode and the circuit mode for a very low value of ε, at which there is no absolute instability. Note that this intersection point is to the left of the peak of the circuit mode. For sufficiently high values of ε there are no real solutions to (4.3) as seen in Fig. 5.3. As ε decreases both dashed lines in Fig. 5.3 will move closer to the beam and circuit modes. For sufficiently small values of ε the blue dashed line will fold over the peak of the circuit mode and have a zero derivative ($\frac{dy}{dx} = 0$) at two points as seen in Fig. 5.4. Therefore there are two solutions that are always complex with nonzero imaginary parts and two solutions that transition from real to imaginary as ε increases.

Figure 5.3: A graphical representation of solutions to (4.2) for the upper band edge for $\varepsilon = 10^{-3}$ where no real solutions exist around the intersection point.

Numerically evaluating the Briggs-Bers criterion for the two roots that are

always complex, in both Figs. 5.3 and 5.4, does not yields absolute instability. Numerically evaluating the Briggs-Bers criterion for the two roots that transition from real to complex as ε increases always yields absolute instability when they are complex. Marginal stability is therefore the point when these two pairs of solutions transition from real to complex. When these solutions are complex they must have the same real parts as argued in C. Therefore, to become real these two pairs of solutions must coincide on the real axis. For each pair of solutions $D(x,y)|_{y_s}$ must have a double x root. However, since these two pairs are the same $D(x,y)|_{y_s}$ must have two double x roots. This means that $D(x,y)|_{y_s}$ has a triple root in x and therefore can be written as

$$D(x,y)|_{y_s} = a(x - x_s)^3(x - b) \qquad (5.38)$$

for some real a and b. This triple root in x at transition to absolute instability may also be seen from Fig. 5.4, where the two double roots on the blue curve must merge to become a triple root before they disappear as ε increases. This appearance of a triple root in x (or in k) is also the threshold condition for the onset of the absolute instability in gyrotron traveling wave amplifier [98], because the latter's dispersion relation is very similar to that of TWT near the upper band edge, as noted in [70]. Using (4.2) to evaluate $D(x,y)|_{y_s}$ and setting each coefficient of the fourth order polynomials of x in Eq. (5.38) equal to each other we obtain a system of five equations with five unknowns (ε, x_s, y_s, a and b). Solving this system yields Eq. (4.5) of the main text.
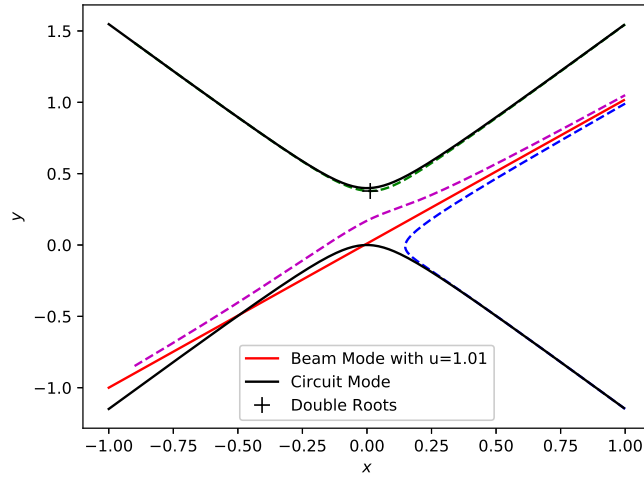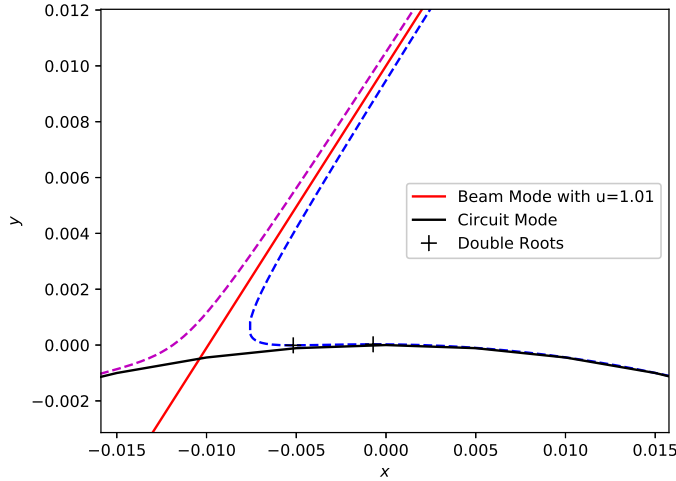

Figure 5.4: A graphical representation of solutions to (4.2) for the upper band edge for $\varepsilon = 10^{-9}$ where no real solutions exist around the intersection point.

References

[1] J. Benford, J. Swegle, and E. Schamiloglu. *High Power Microwaves*. 3rd. CRC Press, 2015.

[2] R. J. Barker and E. Schamiloglu. *High-Power Microwave Sources and Technologies*. 1st. Wiley-IEEE Press, 2001.

[3] R. S. Timsit. *Electrical Contacts: Principles and Applications*. Ed. by P. G. Slade. CRC Press LLC, 1999. Chap. Electrical contact resistance: Fundamental principles, p. 1.

[4] R. Holm. *Electric Contacts: Theory and Application*. 4th. Springer-Verlag, 1967.

[5] *Review of Federal Programs for Wire Systems Safety, Final Report*. Tech. rep. Washington, DC: National Science and Technology Council, Nov. 2000.

[6] M. R. Gomez, J. C. Zier, R. M. Gilgenbach, D. M. French, W. Tang, and Y. Y. Lau. "Effect of soft metal gasket contacts on contact resistance, energy deposition, and plasma expansion profile in a wire array Z-pinch". In: *Rev. Sci. Instrum.* 79.09351 (2008).

[7] M. D. Haworth, G. Baca, J. Benford, T. Englert, K. Hackett, K. J. Hendricks, D. Henley, M. LaCour, R. W. Lemke, D. Price, D. Ralph, M. Sena, D. Shiffler, and T. A. Spencer. "Significant pulse-lengthening in a multigigawatt magnetically insulated transmission line oscillator". In: *IEEE Transactions on Plasma Science* 26.3 (1998), pp. 213–219.

[8] P. Bruzzone, B. Stepanov, R. Dettwiler, and F. Staehli. In: *IEEE Trans. Appl. Supercond* 17.1378 (2007).

[9] H. Gelinck, T. C. T. Geuns, and D. M. de Leeuw. In: *Appl. Phys. Lett.* 77.1487 (2000).

[10] W. J. Greig. *Integrated Circuit Packaging, Assembly, and Interconnections*. Springer, 2007.

[11] L. Carbonero, G. Morin, and B. Cabon. In: *IEEE Trans. Microwave Theory Tech.* 43.2786 (1995).

[12] S. B. Fairchild, J. Boeckl, T. C. Back, J. B. Ferguson, H. Koerner, P. T. Murray, B. Maruyama, M. A. Lange, M. M. Cahay, N. Behabtu, C. C. Young, M. Pasquali, N. P. Lockwood, K. L. Averett adn G. Gruen, and D. E. Tsentalovich. In: *Nanotechnology* 26.105706 (2015).

[13] R. H. Baughman adn A. A. Zakhidov and W. A. de Heer. "Carbon nanotubes - the route toward applications". In: *Science* 297.787 (2002).

[14] D. Shiffler, T. K. Statum, T. W. Hussey, O. Zhou, and P. Mardahl. In: *Mod. Microw. Millim. Wave Power Electron* IEEE, Piscataway, NJ (2005), p. 691.

[15] W. Tang, D. Shiffler, K. Golby, M. LaCour, and T. Knowles. In: *J. Vac. Sci. Technol. B* 30.061803 (2012).

[16] S. Krishnan W. Wu, T. Yamada, X. Sun, P. Wilhite, R. Wu, K. Li, and C.Y. Yang. In: *Appl. Phys. Lett.* 94.163113 (2009).

[17] Z. Yao, C. L. Kane, and C. Dekker. In: *Phys. Rev. Lett.* 84.2941 (2000).

[18] D. Mann, A. Javey, J. Kong, Q. Wang, and H. Dai. In: *Nano Lett.* 3.1541 (2003).

[19] A. Mikrajuddina, F. G. Shib, H. K. Kimb, and K. Okuyama. "Size-dependent electrical constriction resistance for contacts of arbitrary size: from Sharvin to Holm limits". In: *Materials Science in Semiconductor Processing* 2 (1999), pp. 321–327.

[20] K. L. Jensen. *Introduction to the Physics of Electron Emission*. Wiley, 2017.

[21] K. L. Jensen, D. A. Shiffler, I. M. Rittersdorf, J. L. Lebowitz, J. R. Harris, Y. Y. Lau, J. J. Petillo, W. Tang, and J. W. Luginsland. "Discrete space charge affected field emission: Flat and hemisphere emitters". In: *J. Appl. Phys.* 117.194902 (2015).

[22] R. Timsit. *Proceedings of the 54th IEEE Holm Conference on Electrical Contacts*. 2009, pp. 332–336.

[23] M. B. Read, J. H. Lang, A. H. Slocum, and R. Martens. *Proceedings of the 55th IEEE Holm Conference on Electrical Contacts*. 2009, pp. 303–309.

[24] G. Norberg, S. Dejanovic, and H. Hesselbom. In: *IEEE Trans. Compon. Packag. Technol.* 29.371 (2006).

[25] K. Nagashio, T. Nishimura, K. Kita, and A. Toriumi. "Contact resistivity and current flow path at metal/graphene contact". In: *Appl. Phys. Lett.* 29.143514 (2010).

[26] H. Kam, E. Alon, and T.-J. K. Liu. In: *Electron Devices Meet. IEDM 2010 IEEE Int.* (2010), pp. 16.4.1–16.4.4.

[27] S. Datta. *Quantum Transport: Atom to Transistor*. Cambridge U. Press, 2005.

[28] P. Zhang, Q. Gu, Y. Y. Lau, and Y. Fainman. In: *IEEE J. Quantum Electron.* 52.2000207 (2016).

[29] Q. Gu and Y. Fainman. *Semiconductor Nanolasers*. Cambridge U. Press, 2017.

[30] P. Zhang and Y. Y. Lau. "Ultrafast and nanoscale diodes". In: *Journal of Plasma Physics* 82.595820505 (2016).

[31] P. Zhang, S. B. Fairchild, T. C. Back, and Yi Luo. "Field emission from carbon nanotube fibers in varying anode-cathode gap with the consideration of contact resistance". In: *AIP Advances* 7.125203 (2017).

[32] S. Benerjee, J. W. Luginsland, and P. Zhang. "A two dimensional tunneling resistance transmission line model for nanoscale parallel electrical contacts". In: *Sci. Reports* 9.14484 (2019).

[33] S. Benerjee and P. Zhang. "A generalized self-consistent model for quantum tunneling current in dissimilar metal-insulator-metal junction". In: *AIP Advances* 9.085302 (2019).

[34] Y. Y. Lau and W. Tang. "A higher dimensional theory of electrical contact resistance". In: *J. Appl. Phys.* 105.124902 (2009).

[35] P. Zhang, Y. Y. Lau, and R. S. Timsit. "On the spreading resistance of thin film contacts". In: *IEEE Trans. Electron Devices* 59.1936 (2012).

[36] P. Zhang. "Effects of Surface Roughness on Electrical Contact, RF Heating and Field Enhancement", doctoral dissertation". University of Michigan, Ann Arbor, 2012.

[37] P. Zhang, D. M. H. Hung, and Y. Y. Lau. "Current flow in a 3-terminal thin film contact with dissimilar materials and general geometric aspect ratios". In: *J. Phys. D: Appl. Phys.* 46.065502 (2013).

[38] P. Zhang and Y. Y. Lau. "Constriction resistance and current crowding in vertical thin film contact". In: *IEEE J. Electron Device Soc.* 1.83 (2013).

[39] P. Zhang and Y. Y. La. "An exact field solution of contact resistance and comparison with the transmission line model". In: *Appl. Phys. Lett.* 104.204102 (2014).

[40] P. Zhang, Y. Y. Lau, and R. M. Gilgenbach. In: *J. Phys. Appl. Phys.* 48.475501 (2015).

[41] R. S. Timsit. "Electrical contact resistance: Properties of stationary interfaces". In: *IEEE Trans. Compon. Packag. Technol.* 22.1 (1999), pp. 85–98.

[42] R. S. Timsit. "Constriction resistance of thin-film contacts". In: *J. Phys. D: Appl. Phys.* 33.3 (2010).

[43] R. S. Timsit and A. Luttgen. "Temperature distribution in an ohmic-heated electrical contact at high signal frequencies". In: *Appl. Phys. Lett.* 108.121603 (2016).

[44] W. Tang, Y. Y. Lau, and R. M. Gilgenbach. "Lumped circuit elements, statistical analysis, and radio frequency properties of electrical contact". In: *J. Appl. Phys.* 106.084904 (209).

[45] F. Antoulinakis and Y. Y. Lau. "A theory of contact resistance under AC conditions". In: *J. Appl. Phys.* 127.125107 (2020).

[46] V. I. Oreshkin. "Thermal Instability during an electrical wire explosion". In: *Physics of Plasmas* 15.092103 (2008).

[47] T. J. Awe, E. P. Yu, K. C. Yates, W. G. Yelton, B. S. Bauer, T. M. Hutchinson, S. Fuelling, and B. B. McKenzie. "Thermal Instability during an electrical wire explosion". In: *IEEE Trans. Plasma Sci.* 45.584 (2017).

[48] D. D. Ryutov, M. S. Derzon, and M. K. Matzen. In: *Rev. Mod. Phys.* 42.167 (2000).

[49] A. M. Steiner, P. C. Campbell, D. A. Yager-Elorriaga1, K. R. Cochrane, T. R. Mattsson, N. M. Jordan, R. D. McBride, Y. Y. Lau, and R. M. Gilgenbach. "The electro-thermal stability of tantalum relative to aluminum and titanium in cylindrical liner ablation experiments at 550 kA". In: *Phys. Plasmas* 25.032701 (2018). DOI: `https://doi.org/10.1063/1.5012891`.

[50] F. Antoulinakis, D. Chernin, P. Zhang Y.Y., and Lau. "Effects of temperature dependence of electrical and thermal conductivities on the Joule heating of a one dimensional conductor". In: *Journal of Applied Physics* 120.13 (2016), p. 135105.

[51] P. Zhang, Jeongho Park, Steven B. Fairchild, Nathaniel P. Lockwood, Yue Ying Lau, John Ferguson, and Tyson Back. In: *Appl. Sci.* 8.1175 (2018).

[52] M. Pedram and S. Nazarian. In: *Proc. IEEE* 94.1487 (2006).

[53] G. S. Bocharov and A. V. Eletskii. In: *Tech. Phys.* 52.498 (2007).

[54] D. P. Hunley, S. L. Johnson, R. L. Flores, A. Sundararajan, and D. R. Strachan. In: *J. Appl. Phys.* 113.234306 (2013).

[55] S. Hertel, F. Kisslinger, J. Jobst, D. Waldmann, M. Krieger, and H. B. Weber. In: *Appl. Phys. Lett.* 98.212109 (2011).

[56] M.-H. Bae, Z.-Y. Ong, D. Estrada, and E. Pop. In: *Nano Lett.* 10.4787 (2010).

[57] Q. Ma, N. M. Gabor, T. I. Andersen, N. L. Nair, K. Watanabe, T. Taniguchi, and P. Jarillo-Herrero. In: *Phys. Rev. Lett.* 112.247401 (2014).

[58] K. Kuribara, H. Wang, N. Uchiyama, K. Fukuda, T. Yokota, U. Zschieschang, C. Jaye, D. Fischer, H. Klauk, T. Yamamoto, K. Takimiya, M. Ikeda, H. Kuwabara, T. Sekitani, Y.-L. Loo, and T. Someya. In: *Nat. Commun.* 3.723 (2012).

[59] M. J. Kang, E. Miyazaki, I. Osaka, K. Takimiya, and A. Nakao. In: *ACS Appl. Mater. Interfaces* 5.2331 (2013).

[60] Q. Gu, J. Shane, F. Vallini, B. Wingad, J. S. T. Smalley, N. C. Frateschi, and Y. Fainman. In: *IEEE J. Quantum Elect.* 50.7 (2014), pp. 499–509.

[61] L de'Medici. In: *Phys. Rev. Appl.* 5.024001 (2016).

[62] P. Zhang, Y. Y. Lau, and R. M. Gilgenbach. In: *J. Appl. Phys.* 105.114908 (2009).

[63] C. Pérez-Arancibia, P. Zhang, O. P. Bruno, and Y. Y. Lau. In: *J. Appl. Phys.* 116.124904 (2014).

[64] P. Zhang and Y. Y. Lau. "Scaling laws for electrical contact resistance with dissimilar material". In: *J. Appl. Phys.* 108.044914 (2010).

[65] P. Zhang, Y. Y. Lau, and R. M. Gilgenbach. In: *J. Appl. Phys.* 109.124910 (2011).

[66] G. S. Gilmour Jr. *Principles of Traveling Wave Tubes*. Artech House, 1994.

[67] J. R. Pierce. *Traveling Wave Tubes*. Van Nostrand, 1950.

[68] G. W. Gewartowski and H. A. Watson. *Principles of Electron Tubes*. Van Nostrand, 1966.

[69] A. P. Kuznetsov, S. P. Kuznetsov, A. G. Rozhnev, E. V. Blokhina, and L. V. Bulgakova. "Wave Theory of a Traveling-Wave Tube Operated Near the Cutoff". In: *Radiophys. Quantum Electron.* 47.356 (2004).

[70] D. M. H. Hung, I. M. Rittersdorf, P. Zhang, D. Chernin, Y. Y. Lau, T. M. Antonsen Jr., J.W. Luginsland, D. H. Simon, and R. M. Gilgenbach. "Absolute Instability near the Band Edge of Traveling-Wave Amplifiers". In: *Phys. Rev. Lett.* 115.124801 (2015).

[71] F. Antoulinakis, P. Wong, A. Jassem, and Y. Y. Lau. "Absolute instability and transient growth near the band edges of a traveling wave tube". In: *Physics of Plasmas* 25.072102 (2018).

[72] A. Jassem, P. Y. Wong, D. P. Chernin, Y. Y. Lau, F. Antoulinakis, D. Packard, T. A. Hargreaves, and C. M. Armstrong. "Extensions of Johnson's theory of backward wave oscillations in a traveling wave tube". In: *IEEE Trans. Electron Devices* 66.1519 (2019).

[73] L. K. Ang and Y. Y. Lau. "Absolute Instability in a Traveling Wave Tube Model". In: *Phys. Plasmas* 5.4408 (1998).

[74] R. J. Briggs. *Electron Stream Interactions with Plasmas*. MIT Press, 1964.

[75] A. Bers. *Handbook of Plasma Physics*. Ed. by M. N. Rosenbluth and R. Z. Sagdeev. North-Holland, 1983.

[76] S. Humphries. *Charged Particle Beams*. Dover Publications, 2013.

[77] Paul M. Bellan. *Fundamentals of Plasma Physics*. Cambridge U Press, 2006.

[78] D. Chernin, T. M. Antonsen, Jr., and B. Levush. "Exact Treatment of the Dispersion and Beam Interaction Impedance of a Thin Tape Helix Surrounded by a Radially Stratified Dielectric". In: *IEEE Transactions on Electron Devices* 46.7 (1999), pp. 1472–1483.

[79] P. Y. Wong, D. Chernin, and Y. Y. Lau. "Modification of Pierce's Classical Theory of Traveling-Wave Tubes". In: *IEEE Electron Device Letters* 39.8 (2018), pp. 1238–1241.

[80] G. Dohler, D. Gagne, D. Gallagher, and R. Moats. "Serpentine waveguide TWT". In: *IEDM Digest* (1987). DOI: 10.1109/IEDM.1987.191465.

[81] Y. S. Tan and R. Seviour. "Wave Energy Amplification in a Metamaterial based Traveling Wave Structure". In: *Europhysics Lett.* 87.34005 (2009).

[82] P. Wong. "A Contemporary Study in the Theory of Traveling-Wave Tubes". University of Michigan, Ann Arbor, 2018.

[83] A. P. Kuznetsov and S. P. Kuznetsov. In: *Sov. Radiophys. Electron.* 27.1575 (1984).

[84] I. Vyssh and U. Zaved. In: *Sov. Radiophys. Electron.* 23.1104 (1980).

[85] N. O. Bessudnova and A. G. Rozhnev. "The effect of space charge on electron-wave instabilities near cut-off frequencies of the slow-wave structure". In: *Tech. Phys. Lett.* 26.418 (2000).

[86] N. M. Jordan, Y. Y. Lau, D. M. French, R. M. Gilgenbach, and P. Pengvanich. "Electric field and electron orbits near a triple point". In: *J. Appl. Phys.* 102.033301 (2007).

[87] T. Wu, H. Luo, X. Wang, A. Asenov, and X. Miao. "A Predictive 3-D Source/Drain Resistance Compact Model and the Impact on 7 nm and Scaled FinFETs". In: *IEEE Trans. Electron Devices* 67.6 (2020).

[88] Y. Y. Lau, D. Chernin, P. Zhang, and R. M. Gilgenbach. "A voltage scale for electro-thermal runaway". In: *2013 19th IEEE Pulsed Power Conf. PPC* (2013). DOI: `10.1109/PPC.2013.6627601`.

[89] R. S. Timsit and A. Luttgen. In: *Appl. Phys. Lett.* 108.121603 (2016).

[90] N. W. Ashcroft and N. D. Mermin. *Solid State Physics.* 1st. Brooks Cole, 1976.

[91] R. A. Matula. In: *J. Phys. Chem. Ref. Data* 8.1147 (1979).

[92] W. K. H. Panofsky and M. Bander. "Asymptotic Theory of Beam Break-Up in Linear Accelerators". In: *Rev. Sci. Instrum.* 39.203 (1968).

[93] V. K. Neil, L. S. Hall, and R. K. Cooper. In: *Part. Accel.* 9.213 (1979).

[94] A. Chao, B. Richter, and C. Y. Yao. In: *Nucl. Instrum. Methods.* 178.1 (1980).

[95] Y. Y. Lau. "Classification of beam breakup instabilities in linear accelerators". In: *Phys. Rev. Lett.* 63.1141 (1989).

[96] K. R. Chu. "The electron cyclotron maser". In: *Rev. Mod. Phys.* 76.489 (2004).

[97] D. G. Colombant and Y. Y. Lau. "Effects of frequency spreads on beam breakup instabilities in linear accelerators". In: *Appl. Phys. Lett.* 55.27 (1989).

[98] Y. Y. Lau, K. R. Chu, L. R. Barnett, and V. L. Granatsteinu. "Gyrotron travelling wave amplifier: I. Analysis of oscillations". In: *Int. J. Infrared Millimeter Waves* 2.373 (1981).